J. Indian Inst. Sci., July–Aug. 1991, **71**, 383–439.

IISc THESES ABSTRACTS

Thesis Abstract (Ph.D.)

Studies on the reproductive endocrinology of the female bonnet monkey (*Macaca radiata*): Hormonal regulation of follicular maturation, luteal function and implantation by N. Ravindranath.
Research supervisor: N. R. Moudgal.
Department: Biochemistry

1. Introduction

Though considerable information is available on the overall regulation of follicular maturation in the primate including the human, lacunae do exist in our understanding of how gonadotropins FSH and LH regulate this complex event. For example, we do not even know if there is a continuous need for these two hormones throughout the follicular phase (spanning 8–10 days in the bonnet monkey) for regulating follicular maturation. In particular, the role of FSH in the recruitment, selection and growth of the follicle to the dominant stage is poorly understood.

A second equally important event in the reproductive endocrinology of the primate which is poorly understood is the implantation or the process leading to the establishment of pregnancy. In particular, we are still not clear if estrogen, besides progesterone, is required for implantation in the primate and if so the mechanism by which estrogen regulates this complex process.

In the present work an attempt has been made to investigate both these events by using the endocrinologically well-characterized South Indian bonnet monkey (*M. radiata*) as the experimental animal model and antihormones (specific hormone antibodies and synthetic hormone antagonists) as tools to probe the questions raised.

2. Experimental programme

2.1. *Studies on follicular maturation*

The need for follicle-stimulating hormone (FSH) in promoting follicular growth and maturation was studied using a well-characterized FSH antibody raised in a donor male bonnet monkey. The effect the antibody produced depended on the time and dose of administration. Thus larger the dose of FSH antibody administered on day 1 of menstrual cycle, the longer was the period for which follicular maturation process was arrested. However, by using a minimal effective dose of 25 ul/monkey, it was possible to neutralize FSH for a period of 24 h or less.

Normally, the follicular phase of the bonnet monkey extends for a ten-day period from day 1 of menstruation. The first major phase of follicular growth is completed by day 8–9 of the cycle and this becomes evident by measuring serum estrogen levels which reach a peak by day 9 of the cycle. The mid-cycle LH/FSH surge and ovulation follow this in 24 and 36 h, respectively.

The recruitment of the follicles into the cohort that starts growing and maturing every cycle occurs during the beginning of every cycle and not during the luteal phase of the previous cycle as thought by some investigators. Conclusive proof for this was obtained by neutralizing all of the circulating FSH during luteal phase of a cycle and observing for any effect on the follicular phase of the succeeding cycle.

No effect was observed The early cohort (follicles of day 1–4) contains follicles of differential sensitivity to FSH lack. By reducing available FSH level (by giving subminimal doses of FSH antibody–10 ul/day from day 1–4), it was observed that follicular maturation process is hastened, the pre-ovulation estrogen surge occurring on day 5 instead of day 9 of the cycle.

The dependence on FSH appears to reach a critical stage during the mid-follicular phase (days 5–7 of the cycle) The neutralization of FSH on day 5 of cycle induced the follicles under maturation to arrest their growth only temporarily. There was a rebound in their growth phase culminating in one among them reaching a Graffian follicle stage on day 11 of cycle instead of day 9. In contrast, day 6 follicles showed a higher sensitivity to FSH lack leading to initiation of a new set of follicles into growth, one among the new set reaching the Graffian follicle stage 9 days later. However, there were in this group two estrogen peaks, one on day 9 as in normal cycling monkeys and another on day 16. The first Graffian follicle (?) appeared defective and did not ovulate while the second produced 9 days later behaved normally. The effect of FSH deprivation was most pronounced on day 7 when the follicle destined to ovulate underwent atresia showing acute drop in peripheral estradiol levels suggesting that the sensitivity of the follicle to FSH was maximum on that day. The next follicle appeared 9 days later. The follicles between days 8 and 10 of the cycle were once again found to be insensitive to FSH lack. If follicular dominance is considered synonymous with it becoming independent of FSH support, it can be concluded that this state is reached by day 8, but the process of dominance may start by day 6 itself.

An interesting finding of the present study was that FSH deprivation during highly sensitive period of follicle growth (*i.e.*, day 6–7 of the cycle) leads not only to the termination of growth of that follicle but also to aberrant folliculogenesis in the ensuing follicular phase. This follicle took normally 9 days to develop into Graffian follicle and ovulated normally. However, the luteal phase was short suggesting that the corpus luteum could be defective in its functioning. Fertility studies undertaken in monkeys treated with antiserum on day 7 led to confirmation of this premise. The induced short luteal phase defect prevented pregnancy establishment.

2.2. *Studies on regulation of luteal function in the monkey*

Extending the studies on corpus luteum function, it was observed that LH is the primary luteotropin in the primate. FSH deprivation during the entire luteal phase affected neither corpus luteum function in the current cycle nor folliculogenesis in the ensuing cycle. The role of prolactin in the regulation of corpus luteum function could not be unequivocally established. However, transient changes in circulating prolactin levels did not affect the function of corpus luteum. Tamoxifen, an antiestrogen, when administered from day 18 to 30 of the cycle daily at 15 mg/kg/day extended the cycle to 48·7 ± 3·8 days suggesting that estrogen effect is blocked in the corpus luteum by Tamoxifen. This implied that estrogen could be having a luteolytic effect.

2.3. *Establishing a requirement for estrogen for implantation in the primate*

An attempt was made to investigate if estrogen is required for pregnancy establishment in primates. Tamoxifen was used as the probe since it is an estrogen antagonist. The trials conducted in mated monkeys with this compound showed that blockade of estrogen action between day 18 and 30 of mated cycle led to prevention in pregnancy establishment in 9 out of 10 monkeys. The effect of Tamoxifen in the face of additional progesterone supplementation suggested that the action is specific to the drug. The Tamoxifen effect was clearly dose dependent. Presumably Tamoxifen was acting here by blocking estrogen action at the endometrial level. It could be blocking the ability of estrogen to induce and regulate its own as well as progesterone receptor level.

Taking into account its potent antiestrogenic activity and long half-life, Tamoxifen dosage and duration of treatment could be reduced without sacrificing efficacy. Thus, administration of Tamoxifen at 7·5 or 15 mg daily for 5 days (from day 16–20) or at 25 mg on day 14 of the cycle only was equally effective in conferring protection against conception. The experiments with day 14 regimen were of particular interest as the drug was given during repetitive cycles to a group of 5 monkeys. Out of 20 cycles recorded, 17 were ovulatory showing that the drug is not interfering when given in this mode and dose

with ovarian function. These studies clearly bring out that there is a need for estrogen for pregnancy establishment in primates. The possibility of developing this into a potent post-ovulatory contraceptive is highly likely.

4. Conclusion

The current study permitted us to unequivocally demonstrate that the need of FSH for regulating follicular maturation in the primate is restricted to the first 8 days of the cycle. Once follicular dominance is attained (by day 8) and the follicular granulosa cells are programmed to produce estrogen in surge amounts (by day 9) it is presumed that follicular growth comes under the regulation of LH and estrogen. It has been clearly demonstrated that sub-minimal levels of FSH during the early follicular maturation phase do influence the ability of the differentiated granulosa lutein cells to produce progesterone at a later stage but for a shorter duration leading to short luteal phase

The use of Tamoxifen as an antiestrogen has clearly permitted us to demonstrate for the first time that there is a critical need/requirement for estrogen for implantation/pregnancy establishment. The possibility of developing this into a viable contraceptive for women seems highly likely.

References

1. RAVINDRANATH, N., SHEELA RANI, C. S., FLORA MARTIN AND MOUDGAL, N. R. — Effect of FSH deprivation at specific times on follicular maturation in the bonnet monkey (*Macaca radiata*), *J. Reprod. Fert.*, 1989, **87**, 231–241.
2. RAVINDRANATH, N. AND MOUDGAL, N. R. — Luteal phase defect induced by deprivation of FSH at specific period of the follicular phase prevents pregnancy in the bonnet monkey (*Macaca radiata*), *J. Reprod. Fert.*, 1990, **88**, 25–30.
3. RAVINDRANATH, N. AND MOUDGAL, N. R. — Use of Tamoxifen, an antiestrogen in establishing a need for oestrogen in early pregnancy in the bonnet monkey (*Macaca radiata*), *J. Reprod. Fert.*, 1987, **81**, 327–336.
4. RAVINDRANATH, N. AND MOUDGAL, N. R. — In *Development of periimplantation embryos and their environment*, K. Yoshinaga (ed.), 1989, pp 277–288, Alan R Liss, Inc New York

Thesis Abstract (Ph.D.)

Differential gene expression/modulation by estradiol-17ß of the riboflavin carrier protein and cytochrome P450 in the chicken and the rat by J. Ramana Murti.
Research supervisors: P. R. Adiga and G. Padmanaban.
Department: Biochemistry.

1. Introduction

The rapidly growing area of steroid hormone-induced gene expression and the increased current awareness of the potential carcinogenic risk of estrogenic compounds (commonly used in rat contraceptive formulations) have prompted several lines of investigations. The estradiol-17ß-induced riboflavin-carrier protein (RCP) gene expression and the 3-methylcholanthrene (3-MC) activation of the cytochrome P450 locus in the chicken and rat liver have provided convenient and elegant model systems to pursue both lines of research at the genetic level. The results obtained with the chicken and rat model systems have provided fresh perspectives regarding the inherent carcinogenecity of the natural steroid hormone estradiol-17ß and the latent estrogenic character of the polycyclic aromatic hydrocarbon procarcinogen 3-MC, both of which share remarkable structural features.

2. Methodology and results

The cDNA clones for both genes were employed to simultaneously assess the hybridizable hepatic mRNA contents upon administration of estradiol-17β at pharmacological doses.

It was first shown that the immunological and biochemical similarities between the chicken and the rat RCP[1] also existed at the level of RCP mRNA. Again the inductive aspect of the RCP mRNA by estradiol-17β was in parallel with the earlier reports on the increased circulatory levels of RCP[2]. The hybridizable hepatic RCP mRNA content was hormonally dose dependent, the magnitude of the response was sex dependent, while the time course of the response was independent of the hormonal status. However, the qualitative aspects of the hepatic response (*viz.*, sexual dimorphism) was clearly evident, with the female chicken being more efficient in terms of the magnitude of the response.

By simultaneous RNA dot blot analysis of the RCP mRNA content in the total *vis-a-vis* the polysomal RNA, it was demonstrated that the steroid hormone causes a significant mobilization of the specific mRNA into the polysome fraction. This phenomenon was clearly more evident in the female chicken hepatic response, again emphasizing the sexual dimorphic features at the level of *de novo* gene induction.

The sexual dimorphism was more apparent in the rat system. By Northern analysis, the sizes of the major hybridizable RCP mRNA species in the chicken and the rat liver were the same (10S) as that observed in the chicken oviduct. This size was well in agreement with the expected size calculated from the complete cDNA clone for the chicken oviduct RCP. Interestingly, several novel hybridizing RCP mRNA species in the female chicken liver and the fetal rat liver have led to the speculation that RCP genes may constitute a small multigene family. The hybridizable hepatic RCP mRNA content in the rodent estrus cycle appeared to be well in accordance with the well-known circulating estrogen and RCP profiles and the reported estrogen-receptor levels.

Realizing the functional importance of the vitamin carrier in the nutritional supply of riboflavin to the growing conceptus during rodent pregnancy[3], an exciting observation was made, wherein the fetal liver is able to express the RCP mRNA during the late stages of gestation. Beyond parturition, both the maternal and the neonatal rat liver express the RCP mRNA at high levels, again well in agreement with the reported levels of circulatory estrogen and its specific hepatic receptor dynamics during the rodent gestation and early lactation phases. An extended loop of the vecotrial nutrient supply/demand and economic utilization of the vitamin in physiologically encompassed tissues was proposed based on the above exciting findings. Extending this scheme for RCP in its functional role, it was demonstrated, for the first time, that the testicular tissue in the adult rat also harboured RCP mRNA in significant proportions.

The indirect role of estrogenic compounds in the etiology of cancers was suspected hitherto on the basis of structural feature of the carbon skeleton, since remarkable similarities could be discerned with those of polycyclic hydrogen procarcinogens (*e.g.*, 3-methylcholanthrene). Since 3-MC primarily activates the hepatic cyt. P450 locus, it was of interest to evaluate the role of the natural steroid estradiol-17β in the activation/modulation of the same genetic locus. Towards this end, a partial cDNA clone was isolated from an estradiol-17β-treated male chicken liver cDNA library, probed with mixed oligonucleotides. The sequence of the oligonucleotides was determined as a computer-assisted consensus of all known cyt. P450 1A sequences. The clone A61, picked up upon controlled stringency washings, harboured a cDNA insert of 900 bases. Partial restriction mapping and DNA sequencing permitted it to be classified as a Type 1A2 member of the cytochrome P450 superfamily. Since the 1A subfamily members are known to be involved in the oxidative metabolism of polycyclic hydrocarbon procarcinogens, this provided a strong incentive to study the activation of the cyt. P450 1A genetic locus by pharmacological doses of estradiol-17β in the same context (hepatic mRNA preparations) as that of the RCP mRNA accumulation. In all the cases examined, it could be clearly shown that the pharmacological property of the steroid is dominant over the physiological parameter in the early stages of the response. Moreover, by Northern analysis it was demonstrated that the estradiol-17β-induced cyt. P450 mRNA was not identical/similar to that induced by 3-MC alone (in terms of size). It thus raises the exciting possibility[4] that estradiol-17β, at pharmacological doses, reprograms the expression of the cyt. P450 genes into aberrant patterns, which in turn could

be directly involved in the initiation of chemical carcinogenesis. In other words, the above findings may provide a direct method for evaluating the carcinogenic risk of estrogen-based oral contraceptive formulations, at the genetic level. Another exciting finding was that 3-MC does possess a weak estrogenic character in activating the RCP gene in the chicken liver of either sex, quite possibly a reflection on the structural identities between polycyclic hydrocarbon procarcinogens and estradiol-17β.

3. Conclusion

When visualized from an overall perspective, the above findings provide fresh insights into the steroid hormonal regulation of gene expression and the implications of these studies in various physiological contexts, besides providing a genetic basis for an inherent intimate link among differential gene expressions, steroid metabolism, nutrition and cancer risk.

References

1. MUNIYAPPA, K. AND ADIGA, P. R. — Isolation and characterization of riboflavin binding protein from pregnant rat serum, *Biochem J.*, 1980, **187**, 537–540.
2. MUNIYAPPA, K. AND ADIGA, P. R. — Occurrence and functional importance of a riboflavin carrier protein in the pregnant rat, *FEBS Lett.*, 1980, **110**, 209–212
3. MURTHY, C V. R. AND ADIGA, P. R. — Pregnancy suppression by active immunization against riboflavin carrier protein, *Science*, 1982, **216**, 191–193.
4. MURTI, J. R., ADIGA, P. R. AND PADMANABAN, G. — Estradiol 17-β induces polyaromatic hydrocarbon inducible cytochrome P450 in chicken liver, *Biochem. Biophys. Acta*, 1991, **175**, 928–935.

Thesis Abstract (Ph.D.)

Antibodies specific to deoxythymidine 5'-monophosphate: Binding to double-stranded DNA by B. Ramachandran.
Research supervisors: T. M. Jacob and N. Appaji Rao.
Department: Biochemistry.

1. Introduction

Antibodies to nucleic acid and its components serve a wide variety of applications in biological systems[1]. Antibodies raised against protein conjugates of ribo- and deoxyribo-nucleosides and nucleotides have been found to be fairly specific to the respective hapten. These antibodies crossreact with the respective hapten when it is present as part of ssDNA but not of dsDNA[2]. The inability of these base-specific antibodies to interact with dsDNA was according to expectation, because the bases are more accessible in ssDNA in comparison to dsDNA. But it was observed in our laboratory that antibodies raised against the nucleotide haptens dpG, dpC and dpA contain antibody populations that bind to dsDNA and are specific to the respective hapten[3,4]. This type of antibodies appeared to be a useful tool in monitoring the conformation of nucleotide units in the dynamic structure of macromolecular DNA both *in vivo* and *in vitro*. Thus the elicitation and characterisation of dsDNA-binding antibodies specific to dpT which had not been prepared yet were pursued.

2. Experimental programme

dpT, being a hapten, was coupled to carrier proteins using the water-soluble carbodiimide, EDC, to prepare immunogens[5,6]. IgG was prepared by sodium sulphate fractionation. ^{3}H-dpT was obtained from BARC, India. ^{3}H-*E.coli*-DNA was isolated from *E.coli* W3110T$^-$ strain by providing ^{3}H-thymine in the

medium. The 3H-DNA was sonicated and either treated with S_1-nuclease to prepare ^{3}H-dsDNA or heat denatured to prepare ^{3}H-ssDNA Nitrocellulose filter antibody binding assay as described by Humayun and Jacob[7] was the assay extensively used to study the binding of antibodies to radiolabelled ligands. The main approach used for antibody characterization was to determine quantitatively the inhibition caused by different concentrations of non-radioactive nucleosides, nucleotides, dsDNA and ssDNA in the binding of ^{3}H-dpT, ^{3}H-dsDNA, and ^{3}H-ssDNA to the antibodies. This enabled the selective study of populations having the highest affinity to any one of the above three radioactive probes, in presence of the other populations of antibodies

3. Results and discussion

The dpT antibodies elicited by earlier workers[5] were not capable of binding to dsDNA. We succeeded in obtaining dsDNA-binding antibodies using LPH-1500dpT as immunogen. Antibodies from one rabbit showed detectable binding to ^{3}H-*E.coli*-dsDNA, ^{3}H-*E.coli*-ssDNA and ^{3}H-dpT. The binding to *E.coli*-dsDNA was much better compared to ssDNA. The dsDNA-binding populations, when studied for their specificities and affinities, using sheared ^{3}H-*E.coli*-dsDNA as binding probe and non-radioactive nucleosides, nucleotides and DNA as inhibitors, show that antibodies bind to dpT residues on *E.coli*-dsDNA and the phosphate group and sugar moiety are important for the binding in addition to the base. But the antibodies are not capable of binding to most of the dpT residues in *E.coli*-dsDNA.

Binding of sheared *E.coli* ^{3}H-dsDNA with increasing input of antibodies got saturated when 90% of the DNA fragments were unbound. Unbound *E.coli*-DNA fragments recovered from dpT antibody binding assay were deficient in dpT antibody binding. The same amount of natural DNAs inhibited ^{3}H-*E.coli*-dsDNA binding to widely different extents. These results indicate limited number of specific binding sites for dpT antibodies on dsDNA.

The results obtained from the binding experiments with ^{32}p-pBR322 DNA and its restriction fragments show the presence of a different population of dpT antibodies, whose binding to dsDNA is Mg^{2+} dependent, but specific to dpT.

Two probable binding sites for dpT antibodies were found to be 5'TAGTT/AACTA and 5'TAAGC/GCTTA by gel electrophoresis assay using DNA fragments of known sequences. The dpT antibodies might be recognizing a dpT residue on these two sequences, probably because of the unique conformation of the nucleotide and the favourable fine structure of the DNA fragment.

The involvement of tyrosine and histidine residues of dpT antibodies in binding to *E.coli*-dsDNA has been identified using amino-acid-modifying reagent.

References

1. JACOB, T. M. AND SRIKUMAR, C. — *J. Biosci.*, 1985, **7**, 61–73
2. STOLLAR, B. D. — *CRC Crit. Rev. Biochem.*, 1986, **20**, 1–36.
3. JACOB, A. AND JACOB, T. M. — *Nucl. Acids Res.*, 1982, **10**, 6273–6280.
4. JACOB, A. AND JACOB, T. M. — *FEBS Lett*, 1985, **189**, 81–84.
5. HALLORAN, M. J. AND PARKER, C. W. — *J. Immunol.*, 1966, **96**, 373–378.
6. HUMAYUN, M. Z. AND JACOB, T. M. — *Biochim. Biophys. Acta*, 1973, **331**, 41–53.

Thesis Abstract (Ph.D.)

Studies on the mechanism of nestmate discrimination in a primitively eusocial wasp: Implications for the evolution of eusociality by Arun Venkataraman.
Research supervisor: R. Gadagkar.
Department: Centre for Ecological Sciences.

1. Introduction

The evolution of eusociality is perhaps one of the most challenging areas of modern evolutionary biology. An attractive and widely discussed solution to this problem is the haplodiploidy hypothesis that attributes the multiple origins of eusociality to the genetic asymmetry created by haplodiploidy (where a female is related to her super sister by 3/4 and her offspring by 1/2) which is universal in this insect order[1]. A significant problem with this hypothesis, however, is that the genetic asymmetry created by haplodiploidy is often broken down by polyandry (multiple mating by the queen) and polygyny (multiple egg-layers in a colony) It is possible, however, that the genetic asymmetry is effectively restored by discrimination of different levels of genetic relatedness within a colony and preferential altruism towards close kin.

2. Methodology and results

Ropalidia marginata (Lep.) (Hymenoptera· Vespidae) is a primitively eusocial wasp which lacks morphological caste differentiation. Worker behaviour may exist because such genetic asymmetry makes the inclusive fitness of workers higher than that of solitary nest foundresses. But this is only possible if different levels of genetic relatedness within a colony are distinguished because serial polygyny and polyandry are known to break down the genetic asymmetry created by haplodiploidy in this species[2,3]. We therefore decided to test whether levels of genetic relatedness within colonies can be discriminated. *R. marginata*, while otherwise being a good model system for studying the evolution of eusociality, does not mate readily under laboratory conditions. Super sisters and half-sisters, therefore, cannot be produced. Hence, we used an indirect assay to assess the possibility that intra-colony genetic relatedness can be discerned. Using behavioural observations of wasps outside the context of their nests, we demonstrated that female *R. marginata* discriminate nestmates from non-nestmates. To make such a discrimination, however, it was essential that after eclosion, both the discriminated and the discriminating animals were exposed to a fraction of their nests and a subset of their nestmates[4]. These results suggest that both recognition labels and templates are acquired by the wasps, after eclosion, from sources outside the body such as the nest or nestmates thus making it unlikely that super sisters and half-sisters within a colony can be distinguished. Hence, genetic asymmetries, broken down by polyandry and polygyny, are unlikely to be restored by preferential altruism towards close kin. Hence, we recommend caution in ascribing the multiple origins of eusociality in the Hymenoptera to haplodiploidy.

To examine nestmate discrimination in the context of the nest, we introduced 'foreign' wasps into laboratory cages containing apparently healthy nests with adult females. These wasps were both genetic relatives and non-relatives of the wasps in the cage. Some of the relatives and non-relatives were exposed to a fragment of their natal nest and a subset of their nestmates and thus had the potential to acquire recognition labels and templates ('exposed' relatives and 'exposed' non-relatives). Others were removed prior to their natural eclosion and thus denied opportunities to acquire recognition labels and templates ('isolated' relatives and 'isolated' non-relatives). All wasps introduced were older than a month. Even though 46 foreign animals were introduced into one of the three cages, none of them was accepted on to the nests regardless of whether they were exposed or isolated, or whether they were relatives or non-relatives. Based on behavioural interactions between nest animals and foreign animals it was found that nest animals treated exposed relatives significantly more tolerantly than exposed or isolated non-relatives. They, however, did not discriminate exposed relatives from isolated relatives. In addition, isolated relatives were not treated differently from both categories of non-relatives. We thus concluded that tolerance is not sufficient for acceptance which may be governed by different rules.

It seemed logical next to explore conditions under which foreign animals are accepted on to nests. The obvious first choice was to look at the effect of age. We introduced 44 animals between 0 and 29 days old into cages containing unrelated colonies. It was quite evident that wasps equal to or less than 8 days in age had a fair chance of being accepted on to unrelated colonies, whereas animals older than 8 days had virtually no chance of being accepted. Older animals (greater than 8 days) made significantly fewer attempts to join the nests and had a significantly lower rate of success per attempt compared to young animals (less than 8 days). Significantly higher rates of aggression were shown by the nest animals towards older foreign animals. Older animals may not be accepted on to alien nests because they are likely to have well developed ovaries and may pose a greater reproductive threat to the members of the unrelated colony. Younger animals may also be more easily moulded into working for their foster colonies. Indeed, we saw one young accepted animal actively foraging for its foster colony.

Once age was established as a factor allowing wasps to be accepted on unrelated colonies, we next examined whether the social role of a wasp in its natal colony could also be an additional factor governing its acceptance on to an unrelated colony. We, therefore, introduced all wasps from one set of laboratory colonies into cages containing unrelated colonies. Here we obtained the very striking result that the probability of a wasp being killed is negatively correlated with the proportion of time it spent away from, rather than on, its original nest. We also found here that in one experiment an egg-layer of a former colony seemed to be selectively sought out and killed by the animals of the unrelated colony.

To correct for an inherent asymmetry in the previous experiment where one set of animals had their own nest while the other did not, we studied the segregation patterns of wasps from two unrelated colonies released into a common cage. Usually nestmates preferred to associate with each other than with non-nestmates. Mixing of unrelated individuals did occur, however, when one set of animals built a nest while in the other only a few survived and no nest was built. If both sets of wasps built nests mixing was never seen.

3. Conclusions

All the results are consistent with the following hypothetical framework. Nestmate discrimination labels have both an exogenous and an endogenous component and both have to be different between two animals for them to be treated significantly differently. Acceptance of alien wasps on to a colony, however, is not merely dependent on these cues. Additional factors such as age, ovarian development and previous social role are also important if not more so. Cooperation to found new colonies appear to depend on yet another set of rules where the status of an animal (whether it has access to its own nest or not) is probably more important in determining whether it will cooperate with an alien wasp.

References

1. HAMILTON, W. D. — The genetical evolution of social behaviour, *J. Theor. Biol.*, 1964, **7**, 1–52.

2. GADAGKAR, R., CHANDRASHEKARA, K., CHANDRA, S. AND BHAGAVAN, S. — Serial polygyny in *Ropalidia marginata:* Implications for the evolution of sociality, *Proc. Int. Congr. IUSSI,* Bangalore, India, August 2–11, 1990.

3. MURALIDHARAN, K., SHAILA, M. S. AND GADAGKAR, R. — Evidence for multiple mating in the primitively eusocial wasp *Ropalidia marginata* (Lep.) (Hymenoptera; Vespidae), *J. Genet.*, 1986, **65**, 153–158.

4. VENKATARAMAN, A. B., SWARNALATHA, V. B., NAIR, P. AND GADAGKAR, R. — The mechanisms of nestmate discrimination in the tropical social wasp *Ropalidia marginata* and its implication for the evolution of sociality, *Beh. Ecol. Sociobiol.*, 1988, **23**, 453–456.

Thesis Abstract (Ph.D.)

The *nod*D3 gene of *Rhizobium meliloti:* Cloning, regulation and sequence analysis by V. Narayan Iyer.
Research supervisor: G. Ramananda Rao.
Department: Microbiology and Cell Biology.

1. Introduction

In *Rhizobium meliloti* the genes involved in the nodulation process are clustered in an operon, *viz.*, common nod operon. It consists of *nod*A, *nod*B, and *nod*C structural genes transcribed in one direction and the regulatory gene, *nod*D1 in the opposite direction[1]. When *nod*D1 was used as hybridization probe, two other genes termed *nod*D2 and *nod*D3 were discovered. With mutations in both *nod*D1 and *nod*D2 genes, *R. meliloti* exhibited nodulation on alfalfa, though with a significant delay[2]. It was therefore important to study the significance of *nod*D3 gene in detail. The cloning, study of regulation and the sequence analysis of the *nod*D3 gene form the basis of this work.

2. Experimental

The *nod*D3 gene was cloned using standard methods followed in molecular biology[3]. The 11kb *Eco*RI fragment of cosmid clone pEK5022 was cloned into *E. coli* vector pACYC184. This construct termed pNID3 was then physically mapped. A 7·3kb *Bam*HI fragment was subcloned into the broad host range vector, pRK290. This construct was termed pNID6.

The plasmid pNID6 was used to construct a *lacZ* fusion into the *nod*D3 gene by subjecting it to mini-Mu*lacZ* mutagenesis[4]. The *nod*D3: *lacZ* fusion generated was termed pNID12. The effect of combined nitrogen was checked on the *nod*D3 promoter activity using pNID12 and JM61 (*nod*D1: *lacZ*) as control.

The 2·2kb *Cla*I fragment carrying *nod*D3 gene was sequenced[5] and analysed using GCG software[6] on a Micro-VAX computer.

3. Results and discussion

3.1. *Cloning of nodD3 gene of R. meliloti*

The *nod*D3 gene was a part of the cosmid clone pEK5022. The pEK5022 DNA was digested with *Eco*RI and blotted by Southern transfer. The *nod*D3 was localized by using a heterologous *nod*D from the strain MPIK3030 as a probe for hybridization. The resulting plasmid was termed pNID3. The smaller fragments carrying *nod*D3 were localized. It was found that *nod*D3 was present on a 2·2kb *Cla*I fragment or a 2·0kb *Bgl*II fragment.

To facilitate the study of *nod*D3 in the *Rhizobium* background as well, it was subcloned into a broad host range vector pRK290. The plasmid was termed pNID6.

The successful cloning of the *nod*D3 gene makes it possible to now say that *nod*D3 gene is functional[7]. Unlike thought by Gottfert *et al*[2], the *nod*D3 gene was also found to be functionally non-equivalent to the other *nod*D genes[7]. The functional importance of *nod*D has also been investigated in other rhizobia[8], although the localization of the *nod*D is different. Appelbaum *et al*[9] have shown that the two *nod*D genes of *Bradyrhizobium japonicum* also differ in structure and function. The plasmid pNID6 has also been used in elucidating the positive and negative control of *nod* gene expression[10].

3.2. *Construction of gene fusion*

It is well known that the presence of combined nitrogen in soil inhibits nodulation[11]. The level of this regulation is however thought to be host controlled[12]. To enable studies on the effect of combined nitrogen

at the molecular level in rhizobia, the gene expression of *nod*D3 was studied by constructing a *lac*Z fusion (pNID12). The *nod*D3 promoter-directed B-galactosidase activity was inhibited by 87% at the highest concentration of combined nitrogen supplied (100 mM) compared to *nod*D1 which was inhibited 34% only. However, at 70 mM nitrogen the *nod*D3 promoter showed an inhibition of 83% while that of *nod*D1 showed 17%, respectively.

These results indicate that the earlier observations[11] of inhibition of nodulation through nitrite accumulation and toxicity need not be the only mechanism. The inhibition of a master regulatory gene like *nod*D3 of the rhizobia could also lower the degree of successful nodualtion and control the phenomenon.

It also substantiates the earlier result[7] that *nod*D genes are indeed functionally non-equivalent.

3.3 *Sequencing of the nodD3 gene and its analysis*

The *nod*D3 gene sequence analysis shows a homology as high as 90% at the amino-acid level with the *nod*D2 product[2] and about 88% with *nod*D1 product[2]. The homology at the nucleotide level is relatively low (73-75%). Several features like putative-promoter and Shine-Dalgarno sequences, terminator, and nod-box consensus have been examined. Changes in the predicted secondary structure have been evaluated using the Chou and Fasman algorithm.

This has led to an observation that the central region of all *Nod*D proteins is more conserved than the N- or C-terminal regions. Structural motifs like Helix-Turn-Helix have also been localized and their similarity to other such motifs[13] demonstrated clearly. A motif for flavonoid binding has also been proposed which involves Betapleat-Helix-Betapleat (B-H-B) based on the protein structure analysis[14]. A model has been proposed for the general structure-function relationship of *Nod*D proteins.

References

1 JACOBS, T. W., EGELHOFF, T T. AND LONG, S. R — *J Bact*, 1985, **162**, 469–476.

2 GOTTFERT, M., HORVATH, B., KONDOROSI, E., PUTNOKY, P., RODRIGUEZ-QUINONES, F. AND KONDOROSI, A — *J Mol Biol.*, 1986, **191**, 411–420.

3. MANIATIS, T., FRITSCH, E. F. AND SAMBROOK, J — *Molecular cloning: A laboratory manual*, 1982, Cold Spring Harbor Laboratory Press, New York.

4. CASTILHO, B. A., OLFSON, P AND CASADABAN, M. — *J. Bact.*, 1984, **158**, 488–495.

5. SANGER, F, NICKLEN, S. AND COULSON, R. — *Proc. Natn. Acad. Sci. USA*, 1977, **74**, 5463–5467.

6. DEVEREUX, J., HAEBERLI, P AND SMITHIES, O. — *Nucleic Acids Res.*, 1984, **12**, 387–395

7. GYORGYPAL, Z., NARAYAN IYER AND KONDOROSI, A. — *Mol. Gen. Genet.*, 1988, **212**, 85–92

8. BASSAM, B. J., ROLFE, B. G. AND DJORDJEVIC, M. A. — *Mol. Gen. Genet.*, 1986, **203**, 49–57.

9 APPELBAUM, E. R., THOMPSON, D. V., IDLER, K. AND CHARTRAIN, N — *J. Bact*, 1988, **170**, 12–20.

10	KONDOROSI, E., GYURIS, J., SCHMIDT, J., JOHN, M., DUDA, E., HOFFMAN, B., SCHELL, J AND KONDOROSI, E.	*EMBO J.*, 1989, **8**, 1331–1340.
11.	STREETER, J. C	*Pl. Physiol*, 1982, **69**, 1429–1434
12	GIBSON, A. H AND PAGAN, J. D.	*Planta*, 1977, **134**, 17–22.
13.	PABO, C. AND SAUER, R.	*A. Rev. Biochem.*, 1984, **53**, 293–321.
14	CHOTIA, C.	*A. Rev. Biochem.*, 1984, **53**, 537–572.

Thesis Abstract (Ph.D.)

Isolation and characterization of *Oryctes* baculovirus (Indian isolate, OBV-KI) and its use in the biological control of the insect pest *Oryctes rhinoceros*(L.) by K. S. Mohan. Research supervisors: K. P. Gopinathan, J. J. Solomon and N. P. Jayasankar. Department: Microbiology and Cell Biology.

1. Introduction

Oryctes rhinoceros is a major insect pest of coconut and oil palm and is of economical significance as it causes damage to these oil crops[1]. A non-occluded baculovirus has been isolated from the diseased *O.rhinoceros* beetles and larvae. This virus has been designated as the Indian isolate of *Oryctes* baculovirus (OBV-KI). The work deals with the isolation of the OBV, characterization of its genome and constituent proteins and the use of this virus for biological control of the insect pest in Minicoy Island (Lakshdweep group).

2. Materials and methods

OBV-KI was isolated from the wild population of *O. rhinoceros* in Kerala. The type isolate, OBV ($PV505^{2-5}$), was obtained from Dr. A. M. Crawford, DSIR, New Zealand, and was used as a reference for comparison throughout this study. OBV-KI was purified from the excreta of virus-infected *O. rhinoceros* beetles using sucrose-gradient centrifugation and immunoaffinity chromatography. Polyclonal antibodies to purified OBV-KI were raised in rabbits. The viral proteins were characterized by electrophoresis in polyacrylamide gels in the presence of SDS. Viral proteins located on the envelope, capsid and the nucleoprotein core were labelled with ^{125}I after disrupting the virus successively in detergents and 2M NaCl. The DNA-binding protein in the nucleoprotein core was identified by NaCl extraction (1,2 and 4M) of OBV-KI proteins and by probing the isolated polypeptides of KI (by SDS-PAGE) with ^{32}P-labelled fragments KI DNA. The restriction sites of *Sal* I and *Xba* I were physically mapped on KI DNA by the use of Southern hybridizations, sequential double digestions of KI DNA and partial digestions of isolated restriction fragments.

3. Results and discussion

3.1. *Isolation of the virus and OBS-KI field studies as a biocide*

OBV-KI was highly infectious to *O. rhinoceros* beetles and the larvae. Electron micrographs of infected tissue showed OBV-KI as enveloped bacilliform particles (215–240 × 77–108 nm) and they were not occluded in a proteinaceous matrix. The midgut epithelium was the primary tissue supporting viral replication (in natural infection). Immuno-osmophoresis of midgut fluid and the cytopathic features of infected nucleus as shown by Giemsa and immunoperoxidase staining were used for the diagnosis of OBV infection

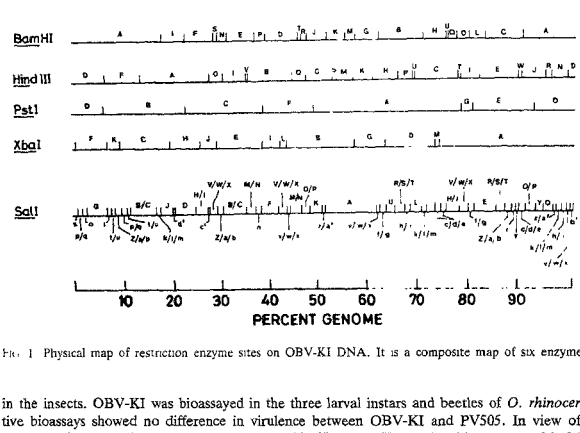

Fig. 1 Physical map of restriction enzyme sites on OBV-KI DNA. It is a composite map of six enzymes

in the insects. OBV-KI was bioassayed in the three larval instars and beetles of *O. rhinoceros*. Comparative bioassays showed no difference in virulence between OBV-KI and PV505. In view of the endemic nature of OBV-KI of disease in Kerala, the field efficacy of KI as a biocide was tested in Minicoy Island. Virus-infected beetles were released into the native pest population of the Island. In the following nine months, the virus disease had spread rapidly and effectively suppressed the pest population to low levels (10% of the initial level) which is being maintained even now. A marked decline in the pest damage to coconut palms was noted.

3.2. *Constituent proteins and comparative ELISA*

The analysis of constituent proteins of OBV-KI by SDS-PAGE and immunoblotting revealed 48 viral polypeptides. Fourteen viral proteins were located on the envelope, and among the nucleocapsid proteins, three were located internally within the capsid. A 235-kDa protein was tightly associated with the viral DNA, which, when isolated, showed DNA-binding property. Comparative studies on OBV-KI and PV505 revealed differences in SDS-PAGE profiles and glycosylation patterns. Immunoblotting of KI and PV505 polypeptides with anti-KI serum demonstrated antigenic differences between the two viral isolates. A modified indirect ELISA has been developed to antigenically differentiate the closely related isolates, PV505 and KI. The antigenic heterogeneity could be quantitated using this assay.

3.3. *Genomic characterization*

The genomic DNA of OBV-KI occurs in the covalently closed, supercoiled conformation. The GC content of OBV-KI DNA has been determined to be 43 mole per cent from thermal melting profiles and by direct base composition analysis using HPLC. Near-total sequence homology of DNA was seen between KI and PV505 from reassociation kinetics. The genomic size of OBV-KI is 83×10^6 Da, corresponding to 126 kbp. Studies with methylation-specific isoschizomeric restriction enzymes did not indicate the presence of any methylated bases in KI DNA. The restriction enzyme cleavage profiles of KI and PV505 DNAs have been obtained with *Eco* RI, *Bam* HI, *Hin* dIII, *Pst* I, *Cla* I, *Sal* I and *Xba* I and the size of KI DNA was computed to be about 123 kbp. Small variations between KI and PV505 in the mobility of one to three restriction fragments were noticed with *Bam* HI, *Eco* RI and *Sal* I. The restriction

enzymes *Xba* I and *Sal* I had 13 and 56 sites on KI DNA. A composite physical map of six restriction enzymes on KI DNA has been presented in Fig. 1.

4. Conclusions

The Indian isolate of OBV could be distinguished antigenically and based on genomic sequences from the type isolate, PV505. The taxonomic status of a variant could be assigned to OBV-KI. The genome of the virus has been physically mapped with respect to six different restriction endonucleases. The potential of OBV-KI as a biocidal agent for the insect pest, *O. rhinoceros*, to contain the crop damage has been established in this study.

References

1. BEDFORD, G. O. — *A Rev. Ent.*, 1980, **25**, 309-339.
2. PAYNE, C. C. — *J. Gen. Virol.*, 1974, **25**, 105–116.
3. PAYNE, C. C., COMPSON, D. AND DE LOOZE, S. M. — *Virology*, 1977, **77**, 269–280
4. CRAWFORD, A M. AND SHEEHAN, C. — *J. Gen. Virol.*, 1985, **66**, 529–539.
5. CRAWFORD, A. M., ASHBRIDGE, K., SHEEHAN, C. AND FAULKNER, P — *J. Gen. Virol.*, 1985, **66**, 2649–2658.

Thesis Abstract (Ph.D.)

Modular design of synthetic protein mimics. Construction of helices by K. Uma.
Research supervisor: P. Balaram.
Department: Molecular Biophysics Unit.

1. Introduction

This work is concerned with the synthesis and structural analysis of peptides designed to adopt specific secondary structures using stereochemically constrained nonprotein amino acids and some specific protein amino acids to direct polypeptide chain folding in the desired fashion as part of a program to develop methods for *de novo* design of proteins. The design of sequences which retain a high solubility in organic solvents further ensures that folding is driven by van der Waals interactions, hydrogen bonding and electrostatic interactions, eliminating hydrophobic interactions as a determinant of the final structure.

Conformational energy calculations[1] first suggested that the α-aminoisobutyric (Aib) residue was likely to favor helical conformations due to the occurrence of deep minima in this region of ϕ, ψ space. Subsequently, a large body of experimental evidence has been accumulated for the ability of Aib residues to stabilize helical structures[2]. In this study, the role of Aib content and positioning on the structural integrity of helices varying in length from 6 to 16 residues has been investigated.

2. Experimental procedures

Peptides have been synthesized by conventional solution phase procedures, using a fragment condensation approach[3] and purified by silica gel column and/or reverse-phase HPLC on a C_{18} column using linear MeOH/H_2O gradients. Solution conformations have been probed by using ^1H nmr and circular dichroism (CD). All the nmr experiments were carried out on a Bruker WH-270 or AMX-400 FT nmr spectrometer as described earlier[3]. CD spectra were recorded on a JASCO J500A spectropolarimeter using 0·1 mm

pathlength cells. Signal averaging was performed and spectra are corrected for the solvent baseline obtained under the same conditions. Crystals were grown by slow evaporation from one or more solvent systems.

3. Results and discussion

Studies on Boc-Air-(Ala-Leu-Aib)$_3$-OMe (ALU-10I) and two isomeric sequences, Boc-Aib-Ala-Aib-Ala-Leu-Ala-Leu-Aib-Leu-Aib-OMe (ALU-10II) and Boc-Aib-Ala-Leu-Ala-Aib-Aib-Leu-Ala-Leu-Aib-OMe (ALU-10III) suggest that the positioning of Aib residues can be switched along the sequence without significantly altering the gross backbone conformation. In the solid state also[4,5], all the peptides are helical, although subtle differences in packing could be observed. While continuous helices have been determined in apolar solvents like $CDCl_3$, partial solvation has been observed in polar, hydrogen-bonding solvents like DMSO and CD_3OD, suggesting environmental effects on helix stability (Fig. 1).

Studies on Boc-(Val-Ala-Leu-Aib)$_n$-OMe (n = 2,4) and Boc-Aib-(Val-Ala-Leu-Aib)$_n$-OMe (n = 2,3) demonstrate that valine residues, which are often considered as β-sheet promoters, can be comfortably accommodated in a helix, in the presence of Aib residues[6-8]. Detailed NOE analysis has been carried out

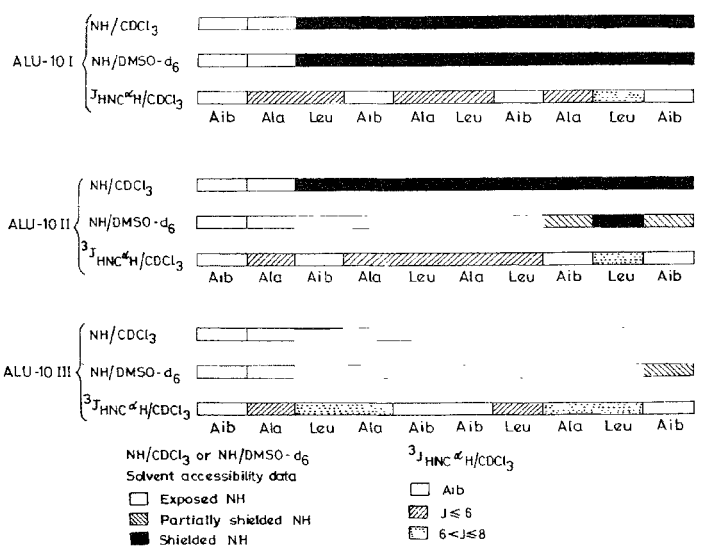

FIG. 1. Summary of the coupling constants data in $CDCl_3$ and NH group solvent accessibility studies in $CDCl_3$ and DMSO−d_6 for the three isomeric peptides ALU-10I, ALU-10II and ALU-10III.

on Boc-Aib-(Val-Ala-Leu-Aib)$_3$-OMe and the results provide firm evidence for a helical conformation in $CDCl_3$. The crystal structure of Boc-(Val-Ala-Leu-Aib)$_4$-OMe reveals that straight helices with no curvature can be constructed in peptides up to 16 residues in length.

The peptides, Boc-Aib-Ala-Leu-Ala-Leu-Aib-Leu-Ala-Leu-Aib-OMe (30% Aib content) and Boc-(Met-Val-Aib-Leu-Ala)$_2$-OMe (20% Aib content), are also largely helical in $CDCl_3$ and DMSO. Observation of both parallel and antiparallel packing of helices for the same peptide suggests that apart from dipole moment other forces might dictate helix aggregation in the solid state[9].

The high potential of Aib residues to nucleate helices has been convincingly demonstrated in the peptides Boc-Val-Ala-Leu-Phe-*Aib*-Val-Ala-Leu-OMe, Boc-Val-Ala-Leu-*Aib*-Val-Ala-Leu-OMe[6] and Boc-(Val)$_2$-*Aib*-Pro-(Val)$_3$-OMe[10], all of which contain only one Aib residue. All the three peptides adopt helical conformations in the solid state and in the apolar $CDCl_3$. However, the helix is significantly destabilized in DMSO in each case, suggesting that a higher Aib content ($\geq$ 20%) is needed to stabilize helices in a variety of environments. Comparison of Boc-Val-Ala-Leu-Aib-Val-Ala-Leu-OMe and Boc-Val-Ala-Leu-Phe-Val-Ala-Leu-OMe clearly establishes the solubilizing and helix-promoting effects of Aib residues. The latter peptide is largely insoluble in $CHCl_3$ and MeOH.

The role of disulfide bridges in stabilizing β-sheet conformation has been established by comparing the cycle hexapeptide Boc-Cys-Val-Aib-Ala-Leu-Cys-NHMe with the acyclic analog. While the former adopts

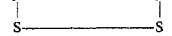

antiparallel β-hairpin conformations[11], the latter is helical in MeOH and $CDCl_3$. Studies on the peptides Boc-Cys-(Val)$_n$-Trp-OMe (n = 1-3) serve to show that Cys residues can be used for stabilizing β-sheet

Boc-Cys-(Val)$_n$-Trp-OMe

conformations in acyclic peptides[12]. Simultaneous observation of both positive and negative NOEs in these peptides provides evidence for segmental motion.

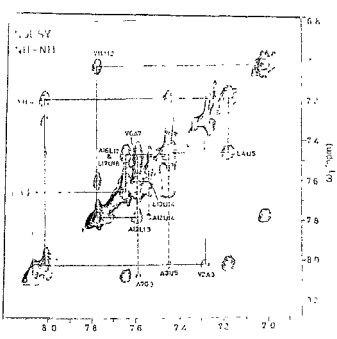

FIG 2. Contour plot of the amide region of the NOESY spectrum of the 18-peptide in $CDCl_3$. Sequential $N_iH \leftrightarrow N_{i+1}H$ NOEs have been traced.

The 18-residue peptide Boc-Aib-Val-Ala-Leu-Aib-Val-Ala-Leu-Gly-Pro-(Val-Ala-Leu-Aib)$_2$-OMe has been synthesized as a model for an αα-motif. A detailed NOE analysis (Fig. 2) and preliminary X-ray structure data suggest that the peptide forms a continuous helix contrary to expectations that the Gly-Pro segment could generate an αα-corner. However, an analysis of the Gly-coupling constants suggests that Gly may be adopting a left-handed helical conformation.

The results, in general, conclusively demonstrate the utility of Aib residues in the construction of stereochemically rigid helical modules. The problems of linker design and control of helix orientation need to be addressed in further developing this approach to *de novo* synthetic protein design.

References

1. MARSHALL, G. R. AND BOSSHARD, H. E. — *Circulation Res.*, 1972, **30/31** (Suppl. II), 143-150.
2. KARLE, I. L. AND BALARAM, P. — *Biochemistry*, 1990, **29**, 6747-6756
3. BALARAM, H., SUKUMAR, M. AND BALARAM, P. — *Biopolymers*, 1986, **25**, 2209-2223.
4. KARLE, I. L , FLIPPEN-ANDERSON, J. L., UMA, K. AND BALARAM, P — *Proc. Natn. Acad Sci. USA*, 1988, **85**, 299-303.
5. KARLE, I. L., FLIPPEN-ANDERSON, J. L., UMA, K. AND BALARAM, P. — *Curr. Sci.*, 1990, **59**, 875-885.
6. KARLE, I. L., FLIPPEN-ANDERSON, J. L., UMA, K. AND BALARAM, P. — *Proteins. Struct , Function Genet* , 1990, **7**, 62–73
7. KARLE, I. L., FLIPPEN-ANDERSON, J. L., UMA, K. AND BALARAM, P. — *Int. J. Peptide Protein Res.*, 1988, **32**, 536-543.
8 KARLE, I. L , FLIPPEN-ANDERSON, J. L., UMA, K. AND BALARAM, P — *Biochemistry*, 1989, **28**, 6696–6701.
9. KARLE, I. L., FLIPPEN-ANDERSON, J. L., UMA, K. AND BALARAM, P. — *Biopolymers*, 1990, **29**, 1835-1845.
10. KARLE, I. L , FLIPPEN-ANDERSON, J. L , UMA, K. AND BALARAM, P. — *Biopolymers*, 1990, **29**, 1433-1442.
11. KARLE, I. L., KISHORE R., RAGHOTHAMA, S. AND BALARAM, P. — *J. Am. Chem Soc.*, 1988, **110**, 1958–1963.
12. BALARAM, H., UMA K. AND BALARAM, P. — *Int. J. Peptide Protein Res* , 1990, **35**, 495–500.

Thesis Abstract (Ph.D.)

Studies on the synthesis and oxidation of substituted hydrazines by D. Chellappa.
Research supervisor: S. R. Jain.
Department: Inorganic and Physical Chemistry.

1. Introduction

Versatility of hydrazines, especially their use as potential liquid rocket fuels, has led to renewal of interest

in their synthetic procedures. Most of the existing methods produce hydrazines as dilute aqueous solutions. Recovery of anhydrous hydrazine from dilute aqueous solution requires multiple distillation, extraction, etc., and, therefore, these processes are cumbersome and expensive. Some of the methods involve carcinogenic substances. Realising this, the synthesis of monomethyl- and unsymmetricaldimethylhydrazine has been attempted recently[1,2] by the anhydrous chloramine process, in non-aqueous solvents. In the present work, adoptability of the anhydrous chloramine process for the synthesis of different types of hydrazines has been examined. Of redox reactions involving hydrazines, the oxidation of hydrazines by oxygen is important due to its extensive application. Further, the reaction plays significant role in storage and utility of hydrazines. In view of these, the present research attempts to explore the oxidation reactions of MMH and UDMH with oxygen in detail.

2. Experimental programme

Gaseous chloramine was generated by the reaction of chlorine and ammonia using a modified generator. Experiments were conducted to study the effect of various parameters, such as the temperature of the reactor wall, time of the experimental run, and the amounts of chlorine, nitrogen and ammonia, to optimize the yield of chloramine. Chloramine generators of various designs were fabricated, and the effect of design on chloramine yield was evaluated. In an effort to synthesize hydrazines and understand the mechanisms of the chloramine and reverse-chloramine processes, chloramination, methyl- and dimethyl-chloramination of amines were attempted. Using gas chromatography, kinetic investigation and product identification of the oxidation of MMH by oxygen was carried out. A similar investigation of the reaction of UDMH with oxygen was also carried out. Specially designed glass vessels were used for the oxidation studies.

3. Results and conclusions

The yield data of chloramine indicate that the introduction of excess nitrogen or ammonia over the stoichiometric equivalent increases the yield of chloramine. The temperature does not seem to have any effect on the chloramine yield in the range 25–95°C. The data indicate that an increase in chlorine input and in the time of the run culminates in a decrease of the chloramine yield. The effects of these parameters have been rationalized, as in an earlier work[3], on the basis of the decomposition of chloramine when it comes into contact with chlorine and ammonia. By optimising the various parameters, it has been determined that the optimum chloramine yield is 63 mmoles. $hour^{-1}$ when the Cl_2:N_2:NH_3 ratio is 1:10:10 corresponding to 134, 1340, 1340 mmoles, respectively. Analysis of the chloramine yield data obtained by generators having different designs reveals that the yield heavily depends on the design of the generator. With a suitably designed generator it is possible to generate chloramine for nearly six hours continuously.

Different kinds of hydrazines, *viz.*, aliphatic, aromatic, heterocyclic, have been prepared by the chloramination of amines taken in non-aqueous solvents, such as ethylene glycol, methanol, etc., having a dissolved fixed base. These include hydrazine, monomethyl-, unsymmetricaldimethyl-, phenyl-, *p*-tolyl-, B-aminoethyl hydrazines, N-aminopyrrolidine, and N-aminopiperidine. The formation of hydrazines has been confirmed by preparing various derivatives and characterizing by ^1H nmr, ir and elemental analysis. The present data show that a fixed base is necessary to generate hydrazines in non-aqueous solvents by the anhydrous chloramine process. The results of the reverse-chloramine process wherein monomethyl-chloramine and dimethylchloramine were reacted with ammonia and other amines further substantiate this result. It is apparent that the undermentioned mechanism which was proposed earlier by Audrieth *et al*[4] prevails in these reactions.

$$NH_2Cl + OH^- \rightarrow NHCl^- + H_2O$$
$$NHCl^- \rightarrow NH + Cl^-$$
$$NH + RNH_2 \rightarrow RNHNH_2$$

The optimum concentrations of the reactants to prepare various hydrazines are given in Table I.

Table I
Yield of different hydrazines

No.	*Hydrazine*	*CA:Amine:Base*	*% yield based on CA*
1	Methylhydrazine	1:8:1·6	70*
2	Dimethylhydrazine	1:6:2·4	70*
3	Phenylhydrazine	1:6:4	70+
4	*p*-tolylhydrazine	1:2·7:2·7	43+
5	B-aminoethylhydrazine	1:4:4	51+
6	N-aminopyrrolidine	1:2:2	85+
7	N-aminopiperidine	1:2:2	50+

CA = Chloramine.
Solvent used: *Ethyl glycol, + Methanol.

The reaction of monomethylhydrazine (MMH) with oxygen has been investigated. Using gas chromatography, nitrogen, methane, water, formaldehydemonomethylhydrazone and methanol are identified as the products of oxidation of MMH. The kinetic data obtained by monitoring the MMH gas chromatographic peak intensity with time lead to the conclusion that the overall order of the reaction is two, the order with respect to each reactant being one. Based on the products formed and the kinetics of the reaction, the following mechanism has been proposed and a rate law based on this mechanism derived.

$$\begin{aligned}
CH_3NHNH_2 + O_2 &\rightarrow CH_3NHNH + HO_2 \\
CH_3NHNH &\rightarrow CH_3 - N = NH + H \\
CH_3N = NH + O_2 &\rightarrow CH_3 + N_2 + HO_2 \\
CH_3 + CH_3N = NH &\rightarrow CH_4 + N_2 + CH_3 \\
CH_3 + O_2 &\rightarrow CH_2O + OH \\
CH_2O + CH_3NHNH_2 &\rightarrow CH_3NHN = CH_2 + H_2O \\
CH_3 + OH &\rightarrow CH_3OH \\
H + HO_2^{\cdot} &\rightarrow H_2O_2 \\
CH_3NHNH_2 + H_2O_2 &\rightarrow CH_3OH + N_2 + H_2O.
\end{aligned}$$

The reaction of unsymmetricaldimethylhydrazine (UDMH) with oxygen leads to the formation of nitrogen, methane, water, formaldehydedimethylhydrazone, tetramethyltetrazene and N,N-dimethylnitrosamine[5]. Here also the oxidation process follows a second-order kinetics, order being one each with respect to oxygen and UDMH. In this case, two plausible mechanisms have been proposed and rate laws derived. Of these mechanisms, one is somewhat akin to that proposed earlier by Mathur and Sisler[5]. In the other mechanism, the methyldiazene formed as a consequent of the reaction reacts further with oxygen giving products similar to those postulated in the case of MMH and O_2 reaction.

References

1. Jain, S. R., Mathur, M. A. and Sisler, H. H. — Synthesis of methylhydrazine in nonaqueous solvents, *Inorg. Chem.*, 1980, **19**, 2192–2195.
2. Sisler, H. H., Mathur, M. A., Jain, S. R. and Greengard, R. — Studies of the chloramination of dimethylamine and 1, 1-dimethylhydrazine, *I&EC Prod. Res. Dev.* 1981, **20**, 181–185.
3. Sisler, H. H., Neth, F. T., Drago, R. S., and Yaney, D. — The synthesis of chloramine by the ammonia-chlorine reaction in the gas phase, *J. Am. Chem. Soc.*, 1954, **76**, 3906–3909.
4. Audrieth, L. F., Colton, E. and Jones, M. M. — Formation of hydrazine from *t*-butyl hypochlorite and ammonia, *J. Am. Chem. Soc*, 1954, **76**, 1428–1431.
5. Mathur, M. A. and Sisler, H. H. — Oxidation of 1, 1-dimethylhydrazine by oxygen, *Inorg. Chem.*, 1981, **20**, 426–429.

Thesis Abstract (Ph.D.)

Studies on dye-sensitized dichromated gelatin for hologram storage by Rupak Changkakoti.
Research supervisors: S. V. Pappu and C. K. Subramaniam.
Department: Physics (Material Science Programme).

1. Introduction

The various techniques of recording wavefront information and retrieving it constitute the total area of holography, the underlying principle of which was invented by Gabor. Holography was dormant for about 12 years after its invention, during which period it was customary to refer to it as 'a solution in search of problems'. It had a second birth when laser appeared on the scene in 1960; and now it looks that no problem is beyond the reach of holography for a solution. For example, problems in such diverse application areas as information display, non-destructive testing (NDT), photonic logic, optical signal processing, optical computing and photonic information storage are being tackled using this technique[1].

Progress in holography strongly depends on the development of better recording materials. A prospective hologram-recording medium, besides being inexpensive, should possess the following important characteristics: sensitivity well matched to available lasers; high spatial resolution, high diffraction efficiency, low noise, linear response and excellent recyclability. Of course, no single material can be expected to meet all these requirements. Gelatin-based silver-halide emulsion (perfected to a high degree of sophistication during the last hundred years) has established its credentials as a worthy hologram-recording medium. Other recording materials that have been under development over the last few decades can be classified as photochromics, photorefractives, magneto-optic materials, photopolymers, electro-optic materials, etc., depending on the physico-chemical properties of the recording medium that are exploited for recording holograms.

Amongst these recording materials, dichromated gelatin (DCG) is found to be an efficient and near ideal medium for recording planar/volume-phase holograms. DCG holograms offer several advantages such as high diffraction efficiency, high signal-to-noise ratio (SNR), and high spatial resolution[2]. A fair amount of research has been done in regard to the characterization and use of DCG in several application areas. In spite of these developments, the widespread use of DCG as a hologram-recording medium is still retarded due to problems such as low energy sensitivity, narrow spectral sensitivity, irreproducibility of results and lack of good understanding of the mechanism of hologram formation.

DCG essentially is sensitive to short wavelength regions of visible light (*e.g.*, blue-green). Some work has been reported about the red light sensitivity of DCG[3]. However, no systematic studies on the characterization of dye-sensitized dichromated gelatin (DSDCG) holograms have been made and hence the present studies were undertaken. This work reports on the dye-sensitized dichromated gelatin for hologram storage with special emphasis on the (i) sensitometric, (ii) recording, (iii) environmental stability, and (iv) reprocessibility aspects of methylene blue-sensitized dichromated gelatin (MBDCG) holograms.

2. Preparation and characterization of MDBCG holograms

With a view to use an inexpensive method of preparing blank gelatin films a non-standard gelatin has been chosen as the base material. A simple ring-casting technique has been employed for getting good-quality gelatin films. Standardised techniques of prehardening and sensitization have been described. Techniques of recording of volume holograms and measurement of their diffraction efficiency have been discussed. The wavelength sensitivity of the MBDCG films is characterized by using optical absorption spectrophotometry. Techniques used for the measurement of vital parameters such as thickness of the films, pH of the processing solutions, relative humidity and frequency of the holographic gratings are discussed in detail.

2.1 *Sensitometric aspects*

Being a chemical process, the MBDCG process is highly sensitive to chemical parameters of the process (*e.g.*, concentration of the chemicals and pH of the solutions used) and therefore investigations to study the influence of these parameters on the performance of MBDCG volume holographic gratings were carried out. In the total process of making MBDCG-based holograms, these parameters have been incorporated at the (i) prehardening, (ii) sensitization, and (iii) post-exposure development stages. The criterion chosen as the figure of merit of their performance is the diffraction efficiency of the gratings as a function of exposure energy (*viz.*, the η *vs* E characteristics). The η *vs* E characteristics of the MBDCG gratings have been obtained as a function of (a) prehardener, and (b) sensitizer concentration. The role of external electron donor, incorporated during sensitization of the films, and the influence of pH of the developing solution on the efficiency of the holograms has been discussed.

2.2. *Recording aspects*

In volume holograms, the Bragg regime of diffraction leads to efficient wavefront reconstruction[5] and such holograms exhibit some special properties such as (i) high diffraction efficiency (η), (ii) angular selectivity (*i.e.*, angular dependence of η as the incident light deviates from the Bragg angle), and (iii) wavelength selectivity (*i.e.*, the dependence of η as the reconstruction wavelength deviates from the hologram construction wavelength). The influence of thickness of the gelatin films and frequency of the recorded gratings on the diffraction efficiency and angular selectivity of the volume gratings has been discussed.

2.3. *Environmental stability and reprocessibility*

The diffraction efficiency of DCG/DSDCG holograms is known to deteriorate on storage under normal temperature and relative humidity. However, the quality of the deteriorated holograms can be restored by reprocessing[6]. Our interest lies in developing environmentally stable DSDCG holograms; hence, a systematic study of the storage life and reprocessibility has been carried out.

3. Conclusions

The study of the influence of (i) prehardening, (ii) sensitizer parameters, (iii) the role of external electron donor, and (iv) pH of the developing solution, on the diffraction efficiency and recording speed of the holograms reveals that (a) the η *vs* E curves are bell shaped thus indicating a nonlinear response of the medium to exposures above a particular value; (b) the degree of prehardening and the sensitizer parameters have influence on the highest peak diffraction efficiency (η_p) and recording speed (S) that can be achieved. A significant conclusion of this investigation is that, unlike the other sensitizers, the presence of an external electron donor does not in any way improve the peak diffraction efficiency (η_p) value[7]. This indicates that for the photoreduction of methylene blue the electrons required are derived from the gelatin itself. The pH of the developing solution is also found to play an equally important role in improving the η_p value of the holograms. Best diffraction efficiency of holograms has been obtained when the pH value is about 6·5 at which value minimum swelling and maximum hardening of the gelatin films were observed. While the thickness variation of the films and frequency of the gratings have no significant influence on the peak diffraction efficiency of the gratings, the angular selectivity however is affected by the variation of thickness and frequency of the record. The study revealed that thicker films or gratings with higher frequency exhibit low angular bandwidth. It is also established that MBDCG medium prepared in our laboratories exhibited uniform frequency response over a frequency range of 800–2600 cycles/mm.

Deterioration of the MBDCG holograms due to environmental factors is found to be significant in the case of holograms having large initial diffraction efficiency in comparison to those having low/medium initial η value. However, the processing of deteriorated holograms enabled 85% restoration of the original η value in the case of holograms with low/medium initial efficiency; but the restoration of the holograms with high initial η value is found to be imperfect. Thus a very good correlation between the environmental stability and reprocessibility aspects of MBDCG holograms has been observed.

A tentative model for the mechanism of the photochemical transformation in the MBDCG medium has been proposed based on the experimental findings and its salient features are the following. The photocrosslinking is initiated by the absorption of radiation by the methylene blue dye. On irradiation, the dye in the MBDCG film goes to an excited state and is then photoreduced by drawing electrons from the gelatin base. The photoreduced dye in turn reduces Cr^{+6} ion to Cr^{+3}, which crosslinks the gelatin chains. The hardening of gelatin due to the crosslinking is believed to be the cause for hologram formation.

References

1 COLLIER, R. J., BURCKHARDT, C. B., AND LIN, L. H. — *Optical holography*, 1971, Academic Press.

2 SMITH, H. M. — *Holographic recording materials*, Topics in Applied Physics, Vol. 20, 1977, pp 75–98, Springer-Verlag.

3 GRAUBE, A. — Dye-sensitized dichromated gelatin for holographic optical equipment fabrication, *Protogr. Sci. Engng*, 1978, **22**, 37–41.

4. RUPAK CHANGKAKOTI AND SASTRY V. PAPPU — Study on the pH dependence of diffraction efficiency of phase holograms in dye sensitized dichromated gelatin, *Appl. Opt.*, 1986, **25**, 798–801.

5 KOGELNIK, H — Coupled wave theory for thick hologram gratings, *Bell Systems Tech J*, 1969, **48**, 2909–2947

6 CHANG, B J — Post-processing of developed dichromated gelatin holograms, *Opt. Commun.*, 1976, **17**, 270–272.

7 RUPAK CHANGKAKOTI, SATENAPALLI S. C. BABU AND SASTRY V. PAPPU — Role of external electron donor in methylene blue sensitized dichromated gelatin holograms: an experimental study, *Appl. Opt.*, 1988, **27**, 324–330.

Thesis Abstract (Ph.D.)

Accurate modeling of terrain undulation and roughness effects on ILS glideslope by M. M. Poulose.
Research supervisors: P. R. Mahapatra and N. Balakrishnan.
Department: Aerospace Engineering.

1. Introduction

At modern airports, aircraft make their final approach for landing along electronically defined glideslopes[1]. Such glideslopes, which are based on the principle of differential depth of modulation (DDM), are subject to aberrations or course bends in the presence of uneven terrain in the vicinity of the installation. Glideslope bends can cause uncomfortable flights or even accidents. Experimental evaluation of the quality of glideslopes is expensive and is not exhaustive. Theoretical modeling of terrain effects overcomes both these drawbacks.

Initially, techniques based on physical optics and physical theory of diffraction were used to model terrain effects on glideslopes. To overcome the shortcomings of these methods, in particular the excessive computational needs, ray-based or geometrical optics-based theories have been used in recent years. The latest in this class are the uniform theory of diffraction (UTD) and the uniform asymptotic theory (UAT).

The theoretical evaluation of the ILS glideslope quality consists of first estimating the total electromagnetic field at the aircraft location due to the antenna assembly in the presence of the terrain and then deriving the DDM which is the final form in which ILS data is presented to the pilot. Both these aspects are considered in this study. The background of various theories and necessary modifications needed for computing the fields generated in the presence of individual terrain elements is presented.

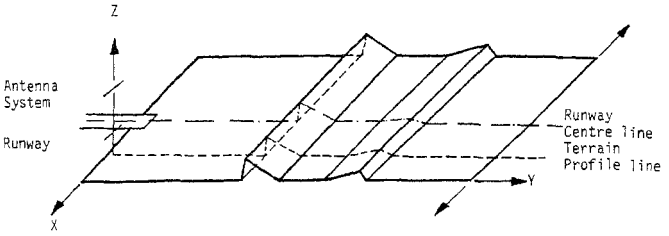

FIG 1 A schematic of 7-plate wedge model for a typical ILS terrain.

2. Terrain modeling and field computation

Successful terrain modeling of real sites, extending over thousands of wavelengths, requires a large number of elements to be examined for their effects, including mutual interactions of high order. To keep the problem tractable, truncations and certain simplifying assumptions are essential. Quite often such are done rather arbitrarily, based on experience. The current study makes an extensive and systematic cataloging of the effect of various terms in each model and of the level of truncation on the overall accuracy/computability tradeoff to lay a scientific basis for the systematic selection of the method of modeling and the threshold of truncation.

The terrain is modeled as piecewise planar surface, *i.e.*, with connected flat plates whose edges are mutually parallel, and perpendicular to the runway centre line. They are assumed to extend to infinity (Fig. 1). The parameters of such a model could be constructed from a contour plan of the terrain or from aerial altimetry along the extended runway centre line.

3. Ray types, their existence and order effects

Determination of ray types is the first major step in the field computation using the ray-theoretic approach. While earlier investigators have made some simplifying assumptions as far as ray groups are concerned, in this study algorithms based on closed form geometric solutions have been developed which exhaustively test for rays of any order including all combinations. This means that the primary three ray types—direct, reflected and diffracted—from each plate and edge can be combined in any order up to any level, and the computer model would automatically check for the existence of the particular combination for the given antenna and observer location. For each ray that is found to exist, the model would proceed to compute the vector field contribution at the observer (aircraft) location.

When the surface impedance of the terrain is negligible, either UTD and UAT may be applied for field computation due to individual rays. Both these have been used in the current work; the UAT has been used for the first time for ILS glideslope application.

Table I
Measured and computed angle parameters in degrees

Parameter	*Measured*	*UAT*	*UTD*
Path angle	3·0	2·98	2·98
Sector width	0·72	0·69	0·676

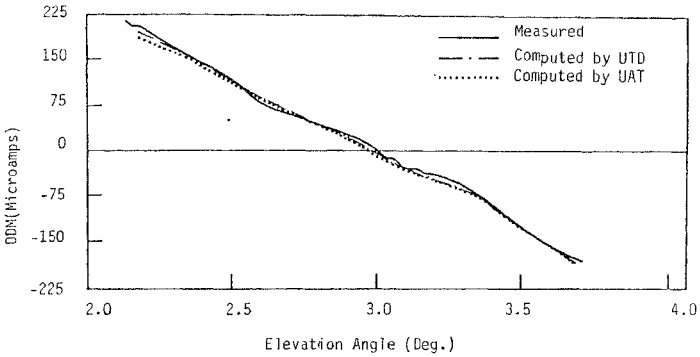

FIG 2. DDM at various elevation angles for a 1000-ft level run at Madras airport

For situations, such as dry and/or sandy terrain, where the surface impedance is significant, a theory to take into account the surface impedance and roughness effects within the framework of the UTD has been developed. The theory is an adaptation of the generalized treatment of impedance wedges and results in a form very similar to the UTD with only one additional factor for the impedance effect.

4. Results: Application to actual airport sites

Following exhaustive ray tracing, field computations have been carried out for the idealized terrain model using UTD, UAT and IUTD techniques developed in the thesis. Rays up to order three have been included. Actual results are generated for three Indian airports — Madras, Hyderabad and Trivandrum. The results from the various techniques are compared. To check the absolute accuracy of the methods, the results are also compared with actual flight test data. Here, as an example, the specific case of Madras is presented, where the operating frequency is 335 MHz and the antenna is located at a distance of about 135 m from the runway centre line. The idealized (piecewise linearized) terrain profile from the antenna location is shown in Fig. 1. Test run results as per ICAO specifications for level flight and low-level approach are used in the study. Results for a 1000-ft level run are shown in Fig. 2. Table I gives a comparison between the measured and computed values.

The computed results are compared with design values for the installation. As against a design glideslope of 3 degrees, a computed glideslope of 2·98 degrees is obtained based on the null at 1000-ft altitude. Further, compared to a measured course width (upper and lower widths combined) of 0·72 degrees, computed course widths of 0·69 and 0·676 degrees are obtained from the UAT and UTD, respectively.

6. Conclusion

The work reported proposes a theory for the modeling of terrain effects on ILS glideslopes and presents actual results demonstrating the validity of the model. The problem is of both theoretical elegance and high practical value because glideslope imperfections have been linked to many air crashes. The experience

gained from this study shows that sophisticated mathematical modeling can yield results very close to true or measured data on the glideslope. Thus modeling can be a low cost, fast and versatile method of site evaluation for ILS installations. Further, the formulation developed in this work can be applied to any general radiating system when scattering and multipath effects are of concern.

References

1. *Installation instruction for ILS*, DOT/FAA No. 6750.6 A, Deptt of Transportation, Federal Aviation Administration, Washington DC, 1969.

2. POULOSE, M. M., MAHAPATRA, P R. AND BALAKRISHNAN, N. Computer aided ILS site evaluation is deemed practical, *ICAO Bull.*, 1986, **46**, 36–39

3 POULOSE, M. M., MAHAPATRA, P R. AND BALAKRISHNAN, N. Terrain modelling of glideslope for instrument landing system, *IEE Proc.*, 1987, **134** (H), 275–279.

Thesis Abstract (Ph.D.)

Studies on strength, behaviour and cracking of lightweight ferrocement in tension and flexure, and pretensioned ferrocement flexural elements by Veerappa Reddy.
Research supervisor: Prakash Desayi.
Department: Civil Engineering.

1. Introduction

Recently, ferrocement has received considerable attention as a possible alternative material for building construction in developing countries. As ferrocement members are thin, thermal comfort is one of the aspects to be considered while adopting this material. To achieve this, sand is replaced by lightweight aggregates. While extensive studies are reported on mechanical properties of ferrocement, no information is available on lightweight ferrocement. Also, the recent trend in construction technology is to evolve materials which are lighter, economical, water proof and are easy to construct and which can be used for roofing of large column-free areas. One of the solutions for this is pretensioning of ferrocement. Taking note of the above points, studies have been conducted on lightweight ferrocement and pretensioned ferrocement elements.

2. Studies on lightweight ferrocement in tension

2 1. *Experimental work*

Lightweight ferrocement is obtained by replacing sand by blast furnace slag from 0 to 100 per cent in steps of 20 per cent. A streamlined shape of the specimen is chosen and uniaxial tension is applied using lazytongs. Meshes used are of two types, of woven mesh 4/20 and 6/22, and the number of layers is varied from 2 to 10. A total of 216 specimens have been cast and tested.

2.2. *Results*

Two parameters, namely, strength-density-parameter, f_w, and specific-surface-parameter, S_p, defined as,

$$f_w = \sqrt{f_{cu}}\,(w/wo)^{3/2} \tag{1}$$

$$S_p = S_L/S_{LM} \tag{2}$$

are introduced to represent replacement of sand and type of mesh. Procedures have been suggested to determine first crack strength, ultimate strength and strain corresponding to ultimate strength. The tensile

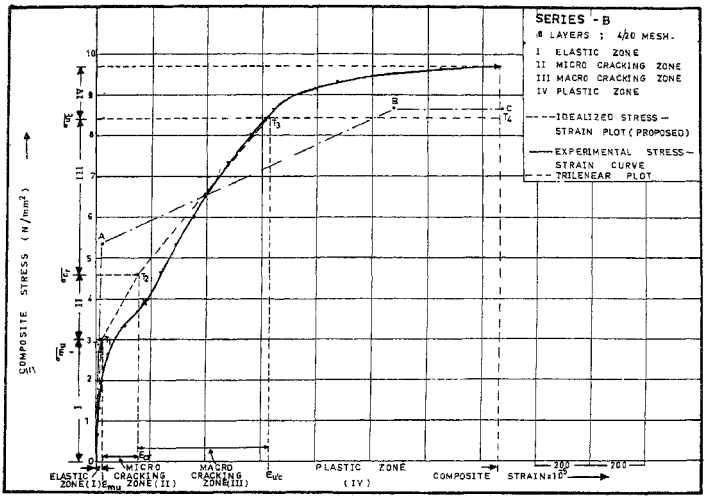

FIG 1 Typical stress-strain curve intension for lightweight ferrocement

stress strain curve is idealized to a plot consisting of four straight lines and the moduli of elasticity in different stages are determined from:

$$Ec_1 = (\sigma_{mu}/\epsilon_{mu}) \tag{3}$$

$$Ec_2 = [\sigma_{cr} - \sigma_{mu})/(\epsilon_{cr} - \epsilon_{mu})] \tag{4}$$

$$Ec_3 = [(\sigma_{u'c} - \sigma_{cr})/(\epsilon'_{uc} - \epsilon_{cr})]. \tag{5}$$

Figure 1 illustrates a typical plot and a comparison with trilinear variations suggested by earlier investigators. Equations have been derived for maximum width (w_m) of cracks appearing on the specimens as,

$$w_m = \frac{K_t \cdot \sigma_{mu} \cdot A_m \cdot \epsilon_e}{K_b \cdot n \cdot \pi \cdot \phi(\sigma_{cr}/\sigma_{u'c})^{\alpha} \cdot f_{bu}}. \tag{6}$$

Constants K_t, K_b and α are determined based on the test data. The computed crackwidths are found to agree satisfactorily with experimental values.

3. Studies on lightweight ferrocement in flexure

3 1 *Experimental work*

To study the flexural strength of lightweight ferrocement, specimens of two sections, namely, rectangular and trough sections have been chosen. Sand has been replaced with foamed blast furnace slag as in the case of tension specimens. The number of layers of 4/22 woven mesh used is 2, 4 and 6 in a 25-mm thick specimen. A total of 108 specimens have been cast and tested.

3.2. *Results*

Modulus of rupture at ultimate (elastic and plastic), deflections, and maximum widths of cracks have been determined and equations proposed to compute the same Variations of f_{ti}/f_w and F_u/f_w with μ have been determined and Fig. 2 shows the latter for illustration. It is noticed that the modulus of rupture ultimate (elastic) is found to depend only on f_w for all values of μ less than 0·12 and it depends on both f_w and μ for all values of μ between 0·12 and 0·7 for both the cross sections. The corresponding values of μ for modulus of rupture ultimate (plastic) are 0·15 and 0·7.

A bilinear equation is proposed to determine the deflections, *viz.*,

$$\Delta_e = \frac{\beta \cdot l^2 \cdot M_{cr}}{E_m \cdot I_g} + \frac{\beta \cdot l^2 (M - M_{cr})}{\alpha \cdot E_{fc} \cdot I_g}. \tag{7}$$

The deflections computed are found to agree satisfactorily with the experimental values.

An equation has been proposed to determine the maximum crackwidth as,

$$w_m = \frac{K_z \cdot f_{ct} \cdot A_e \cdot \epsilon_s}{K_b \cdot (M_{cr}/M_u)^{\alpha} \Sigma \left[f_{bi}(d_i - x)/(d - x)\right] \cdot n \cdot \pi \cdot \phi]}. \tag{8}$$

The constants K_z, K_b and α have been determined from the test data. It is found that the ratios w_m(cal)/w_m(exp) points lie within ± 45 per cent lines of agreement.

4. Studies on pretensioned ferrocement roofing and floor elements in flexure

4.1. *Experimental work*

A trough section is considered for roofing and a channel section for floor as illustrated (Fig. 3). The thickness of the elements is 20 mm in both the cases and the specimens had a span-to-depth ratios of 12, 18 and 24. In each ratio, two prestress values as different eccentricities have been studied. Thus a total of 16 specimens have been cast and tested in flexure.

4.2. *Results*

Methods have been proposed to determine first crack strength, ultimate strength, deflections and maximum widths of cracks. Cracking moment is given by,

$$M_{cr} = ((f_r \cdot I_T)/y_t) + ((f_{pc} \cdot I_T)/y_t). \tag{9}$$

In determining the ultimate moment two different approaches have been used, one based on the prestressed concrete theory and the other as a summation of mortar-mesh and steel bar contributions. The equations obtained for trough sections are:

$$M_u = [(A_z \cdot f_y + A_{zt} \cdot f_{sy})\ (d - d'_2) + A_{st2} \cdot f_{sy}(D/2 - d'_2) - 0{\cdot}68 \cdot f_{cu} \cdot b_w \cdot \times (\beta \cdot x - d'_2)]. \tag{10}$$

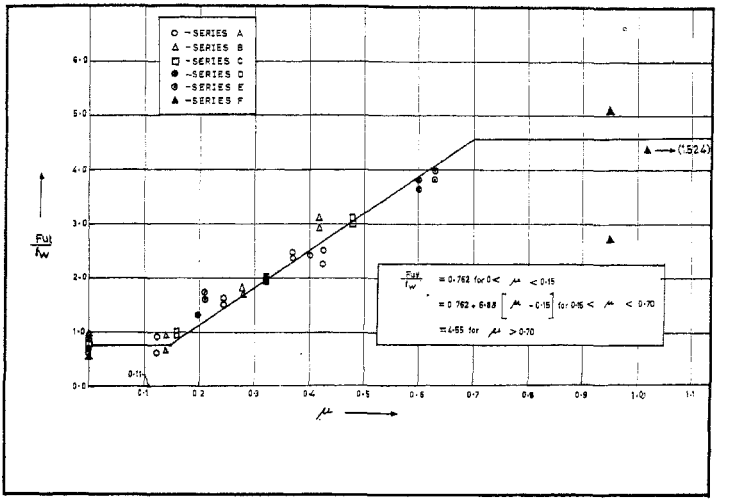

FIG. 2. Modulus of rupture (plastic) at ultimate — trough sections.

Similar equations have been determined for elements of channel sections also.

The equations proposed for deflections and maximum crackwidths are similar to those in equations (7) and (8). All the proposed methods have been found to give satisfactory predictions of the experimental results.

5. Conclusions

1. Equations proposed to compute first crack strength, ultimate strength, deflections and maximum crackwidths in lightweight ferrocement and pretensioned ferrocement have been found to give satisfactory predictions of the experimental results.

2. Proposed equations, tables and charts would be helpful in designing lightweight ferrocement in tension and flexure and pretensioned ferrocement in flexure.

Notation

A_m = Cross-sectional area of mortar
A_s = Area of prestressing wires
A_{st} = Area of nontensioned steel in tension flange

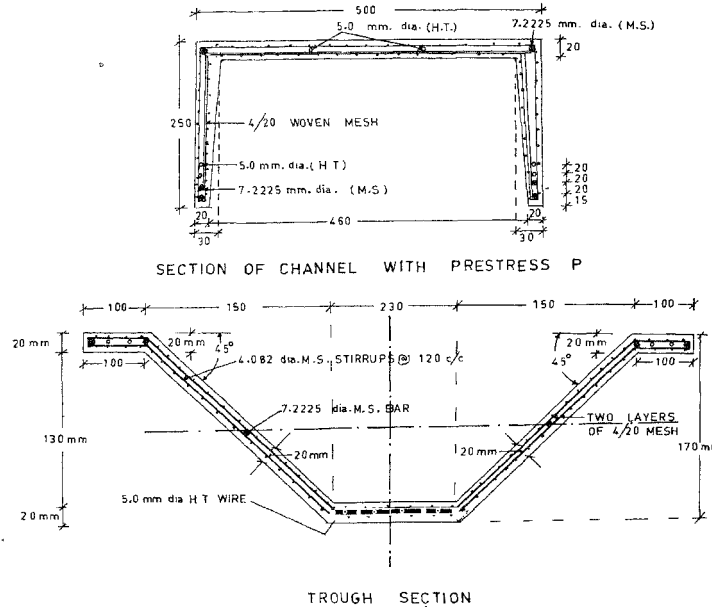

FIG. 3. Cross-sectional details of channel and trough sections

b_w = Breadth of web
D = Total depth of section
d = Effective depth of flexural members
d_1 = Depth of bottom layer of M.S. bars
d_1' = Depth of compression steel in compression flange
Ec_1 = Modulus of elasticity in the elastic range
Ec_2 = Modulus of elasticity in micro cracking range
Ec_3 = Modulus of elasticity in macro cracking range
E_{fc} = Modified modulus of elasticity
Fu = Modulus of rupture (plastic) at ultimate
f_{bu} = Ultimate band stress
f_{cu} = Ultimate compressive strength of 100-mm mortar cube
f_{pc} = Compressive stress in mortar at bottom-most fibre due to prestress
f_{sy} = Proof stress of reinforcement

f_u = Modulus of rupture (elastic) at ultimate
f_r = Modulus of rupture of mortar
f_y = 0·2 per cent proof stress of prestress steel
I_g = Gross moment of inertia of section
K_s = Factor giving average bond stress
K_b = Factor giving average tensile stress
l = Effective span of the specimen
M_u = Ultimate moment
M_{cr} = Moment at cracking
n = Constant
S_L = Specific surface of reinforcement in loading direction
S_{LM} = Minimum specific surface of reinforcement in loading direction
w_o = Density of normal ferrocement
w = Density of lightweight ferrocement
x = Neutral axis depth of cracked section
y_t = Maximum distance of tensile fibre from neutral axis
α = Constants
β = Constant depending on load in deflections
ϵ_e = Strain in mortar
ϵ_{cr} = First crack strain
ϵ_{mu} = Ultimate strain in mortar in tension
ϵ'_{uc} = Strain at ultimate strength of mortar
σ_{cr} = First crack stress
σ_{mu} = Ultimate tensile stress in mortar
$\sigma_{u'c}$ = Ultimate strength of ferrocement
ϕ = Diameter of bar
π = Constant

References

1. DESAYI, P. AND JACOB, K. A. Strength and behaviour of ferrocement in tension and flexure, *Proc. Symp on Modern Trends in Civil Engineering*, Roorkee, India, November 11–13, 1972, pp 274–279.

2. DESAYI, P. AND REDDY, V. Strength and behaviour of lightweight ferrocement in tension, *Proc. Second Int. Symp. on Ferrocement*, 1985, Bangkok, Thailand, January 14–16, 1985, pp 61–73

3. DO TOAN AND PAMA, R. P. A study of flexural cracking and bondslip in pretensioned ferrocement elements, *J. Ferrocem*, 1987, 17, 1–31.

Thesis Abstract (Ph.D.)

Boundary element analysis of linear and nonlinear behaviour of reinforced concrete structures by N. Gopala Rao.
Research supervisors: K. T. Sundara Raja Iyengar and B. K. Raghuprasad.
Department: Civil Engineering.

1. Introduction

The study of linear and nonlinear behaviour of reinforced concrete structures involves several complexities because of which the conventional analysis and design methods are conservative and hence uneconomical. However, with the advent of high-speed electronic computers with immense computational power, new methods such as the finite element method (FEM) and boundary element method (BEM) have emerged

as most popular numerial methods thereby revolutionising the concept of structural analysis and design. Whereas a lot of research work has been reported on the application of finite element method to linear and nonlinear analysis of reinforced concrete (RC) structures, the application of boundary element method to analyse them has not received the attention it deserves from researchers in this area. The present work aims at filling this gap to some extent.

2. Scope

The aim of the study was to develop a suitable algorithm for dealing with the inhomogeneity introduced by the presence of steel reinforcement and then to extend the method for the study of linear and nonlinear behaviour of reinforced concrete structures. The study was carried out in four stages.

(i) Study of linear elastic response of plain concrete structures using BEM.

(ii) Modelling of reinforcement in BEM and studying the linear behaviour of RC structures.

(iii) Analysis of nonlinear response of RC structures using an elastic-cracking constitutive law for concrete and elastic-perfectly plastic law for steel.

(iv) Analysis of nonlinear response of RC structures using an elastic-plastic-cracking constitutive law for concrete and elastic-perfectly plastic law for steel.

The results of research from the above cases are compared with those of other methods, specially the experimental ones, and found to be highly satisfactory.

3. Results and conclusions

3.1. *Study of the linear elastic response of plain concrete structures*

The problem of stress analysis of an unreinforced prestressed concrete anchorage block is chosen for which stresses have been obtained analytically by Iyengar[1]. While studying this problem, the emphasis was on comparison of solutions obtained by different formulations of BEM with the solutions obtained by FEM analysis and analytical solutions. Results show that indirect BEM has given the most accurate results for the problem considered, while those of other methods followed closely.

3.2. *Study of linear response of reinforced concrete structures*

After satisfactory application of BEM to the linear analysis of plain concrete, the more difficult task of representation of steel reinforcement and treatment of consequent inhomogeneity was taken up. The smeared steel concept which is familiar in FEM analysis[2] was adopted to represent steel. Initial stress procedure as outlined by Brebbia *et al*[3] and Telles[4] was used to develop an iterative algorithm to arrive at the final solution. The direct BEM software of Brebbia *et al*[3] for linear elastic analysis of two-dimensional homogeneous regions was used as skeleton program to develop a software for the solution of linear problems in reinforced concrete. Elastic solutions were obtained for the problems of reinforced concrete anchorage block and a singly reinforced beam. It has been observed that the results closely match with that of FEM results, indicating the success of smeared technique and initial stress procedure.

3.3. *Study of nonlinear response of RC structures using elastic cracking material model for concrete and elastic-perfectly plastic model for steel*

The constitutive model for concrete which is used for analysis has been developed by Iyengar and Channakeshava[5]. Cracks were represented using the smeared crack concept. The initial stress procedure[3] was used to develop an incremental iterative algorithm for analysing the nonlinear behaviour. The software was modified accordingly. The software was tested by applying it to two problems — a moderately deep

beam with longitudinal reinforcement tested at Delft University of Technology[6] and shear wall panels tested and analysed by Cervenka and Gerstle[7]. The results obtained closely match those of experiments and FEM analysis.

3.4. *Study of the nonlinear response of RC structures using elasto-plastic-cracking material model for concrete and elastic-perfectly plastic model for steel*

The constitutive law for concrete, which has been modified to include the effect of yielding of concrete in compression, has been developed by Channakeshava and Iyengar[8]. The same initial stress procedure and incremental iterative scheme which have been used for elastic-cracking analysis have been used in this case also. The software was modified to include the modified constitutive law The software was applied to the analysis of shear panels tested by Vecchio and Collins[9]. The results obtained agree with the experimental ones. One interesting observation was made during the course of analysis. In the case of FEM analysis, it has been observed that if all the elements connected to an internal node crack, the stiffness at that point would reduce to zero, thereby rendering the stiffness matrix singular. Such a situation does not arise in BEM analysis. This is one specific advantage of BEM.

4. Conclusions

On the basis of results obtained during the course of the research programme, it may be concluded that BEM formulation involving the initial stress procedure, smeared steel and smeared crack concepts has been successful in solving the linear and nonlinear problems in RC structures. Apart from the advantage of nonsingularity in the solution process, the simplicity of data preparation is most attractive for the practising engineer.

References

1. SUNDARA RAJA IYENGAR, K. T. — Two dimensional theories of anchorage zone stresses in post-tensioned prestressed beams, *J. Am. Concr Inst. Proc.* 1962, **59**, 1443–1466.

2. RASHID, Y. R. — Analysis of prestressed concrete pressure vessels, *Nucl. Engng Des.*, 1968, **7**, 334–344.

3. BREBBIA, C. A , TELLES, J. C AND WROBEL, L. C. — *Boundary element techniques*, 1984, Springer-Verlag

4. TELLES, J. C. — The boundary element method applied to inelastic problems, *Lecture Notes in Engineering*, Vol. 1, 1983, Springer-Verlag

5. SUNDARA RAJA IYENGAR, K. T. AND CHANNAKESHAVA, C. — Elastic-cracking analysis of concrete structures, *Proc. National Seminar on Recent Trends in Structural Analysis and Design*, Bangalore, March 1987, pp A55–A59.

6 DE BORST, R. AND NAUTA, P. — Smeared crack analysis of reinforced concrete beams and slabs failing in shear, *Proc. Computer-aided Analysis and Design of Concrete Structures*, Part I (ed. Damjanic *et al*), 1984, pp 261–273.

7. CERVENKA, V. AND GERSTLE, K. H. — Inelastic analysis of reinforced concrete panels under in-plane loads, *Inelasticity and nonlinearity in structural concrete*, University of Waterloo Press, Study No. 8, Paper 13, pp 333–344, 1972.

8 CHANNAKESHAVA, C. AND SUNDARA RAJA IYENGAR, K. T. — Elasto-plastic-cracking analysis of reinforced concrete, *J. Struct Engng*, ASCE, 1988, **114 (ST-11)**, 2421–2438.

9. VECCHIO, F AND COLLINS, M. P. — *The response of reinforced concrete to in-plane shear and normal stresses*, Research Report, Department of Civil Engineering, University of Toronto, March 1982.

Thesis Abstract (Ph.D.)

Some new addressing techniques for RMS-responding matrix LCDs by T. N. Ruckmongathan.

Research supervisors: B. S. Sonde and V. N. Madhusudana (RRI).
Department: Electrical Communication Engineering.

1. Introduction

Liquid crystal displays (LCDs) constitute an important class of electronic displays and are extremely popular in a wide range of applications. Low voltage operation, low power consumption, low cost, good readability in high-ambient lighting condition and flat-panel construction are some of their major advantages A typical LCD consists of an array of display elements or picture elements (pixels) organised in the form of an X–Y matrix as in the case of many flat-panel displays. The pixels in a matrix display should have nonlinear electro-optic characteristics for being selectively activated or addressed. This is known as matrix addressing and is also referred to as multiplexing. The effectiveness of LCDs in practical applications depends on the efficiency of the pixel as an electro-optic transducer and the addressing technique employed.

Considerable efforts have been directed towards the development of new electro-optic effects and new liquid crystal materials to improve the display characteristics. The twisted nematic LCDs (TNLCDs) and the super-twisted birefringence effect displays (SBE displays) are the two most popular LCDs available today. Both TNLCDs and SBE displays exhibit rms response to applied electric field. Some important characteristics desirable in addressing techniques for those LCDs are·

(i) Good discrimination between the ON and the OFF pixels; this ensures a good contrast ratio in the display. The selection ratio defined as the ratio of the rms voltage across an ON pixel to that across an OFF pixel is a measure of this discrimination and hence it should be high.
(ii) DC-free operation; the display should be addressed with ac fields to ensure long life.
(iii) Low amplitude of addressing waveforms; this reduces the supply voltage requirement of the drive electronics.
(iv) Good pixel brightness unifromity; this ensures uniform appearance of the display
(v) Ease of implementation; this reduces hardware complexity and cost.

The following two approaches are possible for addressing matrix LCDs:

(i) Direct multiplexing, wherein the intrinsic nonlinear characteristics of the pixels are exploited.
(ii) Active matrix addressing, wherein an extrinsic nonlinear element is incorporated in association with each pixel.

Direct-multiplexed displays are popular because of their simple construction, high yield and low cost. Some important developments in direct multiplexing are:

(i) Analysis of scanning limitations of LCDs by Alt and Pleshko[1]. This is a milestone in the addressing of LCDs. The selection ratio of this technique (APT) is a maximum for all values of N, but the supply voltage requirement increases with N. A dc-free operation is ensured by a periodic reversal of the polarity of the row- and column-addressing waveforms which further increases the supply voltage requirement. Displays addressed using APT have a poor brightness uniformity of pixels when N is large.

(ii) New addressing waveforms proposed by Kawakami *et al*[2] are an improvement over those of APT. This technique will be referred to as improved Alt and Pleshko technique (IAPT). It achieves the same selection ratio as in APT and a dc-free operation, but, requires a lower supply voltage than APT. The brightness uniformity of pixels in displays addressed using IAPT is also poor when N is large.

(iii) Addressing method for non-multiplexed liquid crystal oscilloscope display proposed by Shanks and Holland[3] can be used to display a single waveform with an infinite selection ratio and will be referred to as pseudo random technique (PRT). The supply voltage requirement of this technique is almost independent of N.

In the present state of the art, the IAPT is widely used to address matrix LCDs for displaying general patterns. Although it is well known that the selection ratio cannot be improved over that of APT or IAPT, there is scope for improvement in the following areas:

(i) Reducing supply voltage requirement;
(ii) Obtaining good brightness uniformity of pixels; and
(iii) Lowering of hardware complexity of the drivers.

In addition to this, the selection ratio of any new addressing technique should not be significantly lower than that of APT or IAPT, especially when N is large.

In the case of displaying restricted patterns, the PRT proposed by Shanks and Holland[3] is suitable for displaying a single waveform with an infinite selection ratio. Only one pixel is selected in each column here. However, the horizontal resolution or the selection ratio is compromised if multiple waveforms are to be displayed. There is scope for increasing the selection ratio even when the number of selected pixels in each column is more than one. Any new addressing technique with a higher selection ratio and without any compromise in the horizontal resolution will be useful for displaying multiple waveforms in oscilloscopes and logic analysers.

Therefore, an in-depth study of the addressing techniques for rms-responding LCDs was undertaken to achieve these goals. New addressing techniques developed as a result of this study are outlined below.

2. New addressing techniques for displaying general patterns

All the new addressing techniques developed for displaying general patterns are based on selecting more than one address line at a given instant of time. This is in contrast to the line-by-line scanning in the conventional techniques like APT and IAPT. The salient features of the new addressing techniques are given below:

(1) Binary addressing technique (BAT) is suitable for matrix LCDs with a limited number of address lines[4]. The supply voltage requirement of this technique is lower as compared to that of IAPT. The hardware complexity of drivers in BAT is also lower than that of IAPT, since only two voltage levels are required in the addressing waveforms as compared to four in the case of IAPT. The lower selection ratio of BAT as compared to IAPT is not a serious drawback since N is small when BAT is used.

(2) Hybrid addressing technique (HAT) extends the BAT for higher values of N[5]. The supply voltage requirement of HAT is lower as compared to IAPT for limited values of N. However, the selection ratio of HAT is lower than that of IAPT.

(3) Improved hybrid addressing technique (IHAT) achieves the same selection ratio as that of IAPT[6]. IHAT is a generalized form of APT wherein a group of address lines is selected simultaneously instead of line-by-line selection as in APT. The supply voltage requirement here is considerably lower than that of IAPT for a wide range of N when more than three address lines are selected simultaneously. The hardware complexity of this technique increases with the number of address lines (ℓ) selected at a given instant of time.

(4) IHAT-S3 and IHAT-S4 are special cases of IHAT with considerable reduction in the hardware requirement of drivers as compared to IHAT, when ℓ is even odd. A good reduction in the supply voltage requirement is possible as compared to IAPT for a wide range of N without significant reduction in the selection ratio using IHAT-S3 and IHAT-S4.

3. New addressing techniques for displaying restricted patterns

The restricted pattern addressing techniques (RPATs) are based on line-by-line scanning as in the case of APT and IAPT. A selection ratio which is independent of the matrix size is achieved in these techniques by altering the column waveforms as compared to the conventional techniques. The selection ratio depends on the number of selected pixels in each column.

- RPAT-NC leads to a negative contrast mode with bright selected pixels against dark background pixels in TNLCDs[7]. The RPAT-NC is a more generalized form of pulse coincidence technique (PCT) proposed by Shanks *et al*[8]. The selection ratio of RPAT-NC is higher than the conventional techniques.

- RPAT-PC leads to a positive contrast mode with dark selected pixels against bright background pixels in TNLCDs. The selection ratio of RPAT-PC is lower compared to RPAT-NC.

4. Conclusion

All the new addressing techniques proposed have been analysed to identify their merits and demerits in comparison to the conventional techniques. These techniques have also been implemented to experimentally verify the results. The new addressing techniques proposed provide better results in several areas as compared to the conventional techniques. The development of generalized addressing techniques for both general and restricted patterns has led to a better understanding of the problem of matrix addressing of rms-responding devices. Availability of these new addressing techniques will hopefully enhance the use of rms-responding LCDs and increase the choice and the trade-off in the selection of a suitable addressing technique for a given application.

References

1. ALT, P. M. AND PLESHKO, P. — Scanning limitations of liquid crystal displays, *IEEE Trans.*, 1974, **ED-21**, 146–155.

2. KAWAKAMI, H., NAGAE, Y. AND KANEKO, E. — Matrix addressing technology of twisted nematic liquid crystal display, *SID-IEEE Rec of Biennial Display Conf.*, 1976, pp 50–52.

3. SHANKS, I. A. AND HOLLAND, P. A. — Addressing methods for non-multiplexed liquid crystal oscilloscope displays, *SID Int. Symp. Dig Tech. Pap.*, 1979, pp 112–113.

4. MADHUSUDANA, N. V AND RUCKMONGATHAN, T. N. — A convenient multiplexing scheme for addressing liquid crystal matrix displays, *Proc Int Liquid Crystals Conf.*, Bangalore, December 1979 (ed. S Chandrasekhar), 1980, pp 409–503, Heyden.

5. RUCKMONGATHAN, T. N. AND MADHUSUDANA, N. V. — New addressing techniques for multiplexed liquid crystal displays, *Proc SID*, 1983, **24**, 259–262.

6. RUCKMONGATHAN, T. N. — A generalized addressing technique for rms-responding matrix LCDs, 1988 *Int. Display Res. Conf. Rec.*

7. RUCKMONGATHAN, T. N. — An LCD for multitrace oscilloscopes, *1986 SID Int. Symp. Dig., Tech. Pap* Vol. 17, *SID 86 Dig.*, pp 128–131.

8. SHANKS, I. A. HOLLAND, P. A. AND HUGHES, A. J. — Liquid crystal oscilloscope displays, *SID Int. Symp. Dig. Tech. Pap.*, 1978, pp 98–99.

Thesis Abstract (Ph.D.)

Source location by signal subspace techniques and ambient noise modelling in shallow water by P. G. Krishna Mohan.
Research supervisor: P. S. Naidu.
Department: Electrical Communication Engineering.

1. Introduction

Source localization in shallow water, by signal subspace techniques, is difficult due to coherent multipath[1] resulting in non-planar wavefronts across the array. Also, the noise in shallow water is largely generated

due to wind action at surface[2]. Such a background noise is no longer white and uncorrelated among the sensors of an array, as required by signal subspace method. A knowledge of the noise coherence is necessary for satisfactory application of signal subspace method[3]. This work looks at these two problems.

2. Source location algorithm

Initially, an algorithm, based on signal subspace approach is developed for localization of a sound source in shallow water using a vertical array. The background noise is assumed to be spatially white. The algorithm makes use of *a priori* knowledge about the spatial distribution of all images due to reflections at the boundaries and the reflection characteristics of the bottom. Also, it is assumed that the spectral matrix of received data is known exactly.

It is observed that the range and depth can be estimated accurately with large and sharp peaks, when the channel is known completely. A source near the surface also can be detected with sharp peak, at least 40 dB above the maximum side lobe occurring at the surface. Thus, the present algorithm makes source localization possible near the surface unlike that of Klemm[4], and range estimation does not have any ambiguity. Further, the algorithm can be used to estimate the parameters of a close source and for estimation of source parameters in deep water and channel with absorbing bottom.

The effect of some of the points that influence the performance has been studied. It is observed that when all significant images which contribute most of the power to the array are considered, the algorithm gives the true estimates of source parameters with a source to side lobe ratio > 40 dB, and the number of significant images can be estimated from the observed data, without knowing the source position. The algorithm is robust against small variations in the medium resulting in incoherence between multipath. But the method is sensitive to bottom velocity variations which can be used effectively to estimate true bottom velocity. Further, the algorithm is modified so that one can estimate the source without having any *a priori* knowledge about the bottom characteristics. But it requires an array having more elements than the number of significant images in the channel.

3. Noise model

Later, a generalized model for surface-generated noise is developed following the works of Buckingham[5] and Oboznenko[6]. The surface noise is modelled as a continuum of point sources, distributed over a sector of an annular ring which can be reduced to common geometries, *viz.*, ring, disc or infinite plane of noise distribution and the noise sources are assumed to have general spatial spectral characteristics. The expressions for spectrum and cross-spectrum between two sensors, placed on vertical axis passing through the centre of noise surface have been arrived at for different geometries. The main observations are summarized as below.

The spectrum is inhomogeneous in shallow water The coherent noise sources, modelled as directional monopoles[5], further increase the inhomogeneity with directionality. The spectral power in soft bottom channels decreases with increase in directionality, while in hard bottom channels it increases with increase in directionality. The coherence is complex when the noise disc radius is small, but it becomes real for large disc sizes. For a given noise plane, the coherence increases with increasing directionality. The noise plane radius, for which the coherence becomes real, is about 10–50 times the channel depth. The coherence is independent of noise sources lying outside a disc of radius equal to inverse of attenuation coefficient in the channel.

4. Performance of new algorithm in the presence of surface noise

Finally, the performance of the signal subspace algorithm has been studied in the presence of surface-generated noise background. We have confined to a specific model of the surface-generated noise, namely, distribution of uncorrelated noise sources over a large disc.

The algorithm performs reasonably well with a source peak to side lobe ratio, greater than 1 dB, when the SNR is greater than 10 dB. It is observed that the performance of the method improves with an increase in peak to side lobe ratio, whenever averaging over all those noise vectors which are least influenced by the background noise is carried out.

Further, for a given source position the performance of the subspace algorithm is better, when the array is located near the surface compared to its position in the middle or at the bottom of the channel. When the array is near the surface it is shown that the improved performance is due to the fact that a fewer images are influenced by the noise arriving through a narrow angular cone. The angular width of the cone becomes large near the bottom and hence it affects a larger number of significant source images, causing a deterioration in the performance of the algorithms.

References

1. URICK, R. J. — *Principles of underwater sound for engineers*, First edn, 1967, McGraw-Hill.

2. WENZ, G. M. — Acoustic ambient noise in the ocean: spectra and sources, *J. Acoust. Soc. Am.*, 1962, **34**, 1936–1956.

3. BIENVENU, G. — Influence of the spatial coherence of the background noise on high-resolution passive methods, *IEEE Proc. on ICASSP*, 1979, pp 306-309.

4. KLEMM, R. — Range and depth estimation by line arrays in shallow water, *Signal Processing*, 1981, **3**, 333–344.

5. BUCKINGHAM, M. J. — A theoretical model of ambient noise in a low-loss shallow water channel, *J. Acoust. Soc. Am*, 1980, **67**, 1186–1192.

6. OBOZNENKO, I. L — Spatial correlation of surface noise in a depthwise-inhomogeneous waveguide with losses, *Sov. Phys. Acoust.*, 1982, **28**, 154–157.

Thesis Abstract (Ph.D.)

Some aspects of vibration of high voltage overhead transmission line conductors by T.V. Gopalan.
Research supervisors: S. Durvasula and G. R. Nagabhushana.
Department: High Voltage Engineering.

1. Introduction

Stranded conductor is invariably used in overhead transmission lines due to its flexibility compared to solid conductors. In spite of the excellent service record of these conductors occasional fatigue failures do occur. The majority of fatigue failures is known to be caused by the dynamic stresses due to aeolian vibration. In this work, several aspects of aeolian vibration of transmission lines are investigated.

2. Investigations

2.1. *The dynamic flexural rigidity conductor $(EI)_d$ of ACSR (aluminium conductor steel reinforced)*

$(EI)_d$ is calculated on the basis of the hypothesis[1] that the outer strands respond independently while the other strands respond monolithically to aeolian vibration. Computed values of $(EI)_d$, using this hypothesis, are found to be in good agreement with experimental values. This model also explains the higher endurance of single aluminium layer ACSR conductor, fatigue failures of multilayer ACSR conductor originating with inner strand failure and the choice of outer strand radius for maximum fibre distance in field dynamic strain measurements, as recommended by IEEE.

2.2. *Influence of conductor current on its self-damping*

Self-damping in ACSR is known to be adversely affected by the current carried by it. Investigations by indoor laboratory tests showed that the reduction in damping at high current was very significant[2].

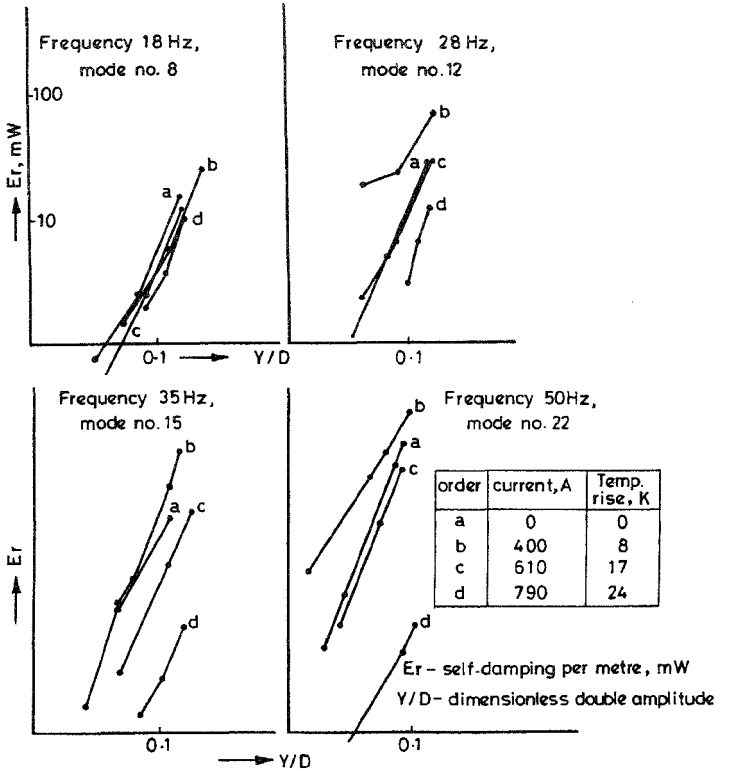

FIG. 1. E_r–Y/D for ASCR moose conductor, tension 25% UTS.

In an ACSR moose conductor, the reduction was about 80% for a current density of 1·54 amp/min^2.

Figure 1 shows E_r–Y/D relation for ACSR moose conductor (54/7/3·53 mm) at conductor currents of 0, 400, 610 and 790 amp for a conductor tension of 20% ultimate tensile strength. This implies that external damping is necessary for many lines which are considered to be satisfactory from the point of view of dynamic performance.

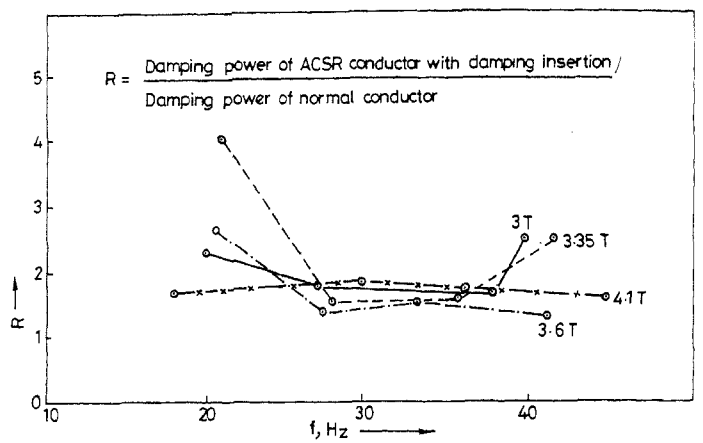

FIG 2. R, f relation of ACSR moose conductor.

2.3. *Improvement in conductor self-damping*

The possibility of enhancing the basic self-damping of ACSR by a 40-micron-thick PVC tape layer inserted between the ultimate and the penultimate layers was attempted[3]. Laboratory investigations showed that the increase in self-damping is at least 70% and the highest is about 300%.

Figure 2 shows the relation between the ratio of damping power of ACSR moose conductor with damping insertion to that of normal moose conductor (R) and the excitation frequency (f) at various conductor tensions.

2.4. *Establishing the reationale of LS model testing*

Length-scaled-down (LS) span, measuring at least 30 m, as per the recommendations of various bodies, has been widely used for investigations on the dynamics of transmission line conductor with and without dampers. In this work, the rationale of reduced span length was arrived at analytically, based on the need to reproduce the lowest aeolian vibration frequency of interest and the effect of catenarity of span.

2.5. *Evaluation of vibration dampers and wind tunnel testing*

A variety of dampers are available to supplement the conductor self-damping, if required. It is necessary to ensure their performance and suitability for specific requirements. A few existing methods of evaluation of dampers have been examined in this work. The ISWR technique[4], standardised by BPA and Indian Standards Institution, is found quite appropriate. The effectiveness of damper was also established by distributed excitation as in the field, on a 24-m LS span in the moderately large inlet section of an open circuit wind tunnel. The action of Stockbridge damper in bringing down the conductor vibration level, the extent of reduction, the need for fine-tuning of resonance in such tests, etc., are highlighted.

2.6. *Limiting conductor static stresses*

The role of static stresses in reducing the conductor fatigue was investigated and the effectiveness of two devices[5], namely, shims and visco-elastic materials, was evaluated by simulated static tests. The results

show that a reduction of about 15% in static strain is possible which would mean an increase in conductor life by about 3 million cycles.

2.7. Nomogram and computer program

The practising engineer normally needs a quick method of assessing the vibration problem and the level of protection required in different field situations. To meet these requirements, nomograms and computer programs are developed. The nomograms are based on both practical experience and theoretical considerations[6]. The computer program is for calculation of vibration level, dynamic bending strain, strain at any point on the conductor, etc., with and without the damper.

3. Conclusions

(a) The mathematical model for $(EI)_d$ developed in this work can be used in vibration analysis of ACSR conductors.

(b) The traditional practice of using 30-m-long length-scaled-down-model span for laboratory tests on conductors and accessories is valid.

(c) Self-damping of ACSR conductor reduces significantly when the conductor carries current; about 80% for a current of 800 amp. It can, however, be improved by insertion of damping tape between the ultimate and the penultimate layers.

(d) ISWR testing is recommended as the best method of evaluation of vibration damper. Wind-tunnel testing of conductor span proves to be a useful tool in the evaluation of conductors and dampers.

(e) Neoprene/spring shim lining in suspension clamp is recommended for reducing conductor static strains and to improve the conductor fatigue life.

(f) Nomogram and computer program are developed for ready and effective use by engineers in the field of assessing the conductor vibration level and the level of protection needed by means of conventional dampers.

References

1 GOPALAN, T. V. AND NAGABHUSHANA, G. R. — Flexural rigidity of stranded cables, *Shock Vibr. Dig.*, 1985, **17**(6), 17–20.

2. GOPALAN, T. V. — Influence of electrical loading on conductor on self damping and dynamic flexural rigidity, *CIGRE*, 1986

3 GOPALAN, T. V., DURVASULA, S., NAGABHUSHANA, G. R., RAO, G. V., MANJUNATH, K. D., AND MANOHARA, K. — Development of ACSR self-damping conductor, *National Seminar on Electrical Power Engineering*, Central Power Research Institute, Bangalore, 1984.

4. GOPALAN, T. V. — A technical note on evaluation of dampers, *Shock Vibr. Dig.*, 1983, **15**(11), 3–4.

5. GOPALAN, T. V., GIRISH, S. AND RAMACHANDRAN, N. — Reduction of static strain for increased life of transmission line conductors, *Strain*, Aug. 1983.

6. LAMPRECHT, A., PHILIP, D., WATTS, I., ROUGHAN, J. AND GOPALAN, T. V. — *The fatigue life of overhead line conductors*, 1982, Report–1864/9/VIII, Dulmison Pty Ltd, Weong, Australia.

Thesis Abstract (Ph.D.)

A search for a short-term ageing test for partial discharge ageing of thin-insulating films by V. Krishnan.
Research supervisors: R. S. Nema.
Department: High Voltage Engineering.

1. Introduction

Polypropylene film is being used widely as a dielectric in high-voltage power capacitors. The design stress is of the order of 600 kV/cm. At this stress, one of the major causes of failure of capacitors is partial discharge. In these capacitors, the outer turns are not as tight as the inner ones and as a result gaseous gaps between the films exist and hence partial discharges are more probable in the outer turns[1]. It is also possible that these air gaps may be at different sub-atmospheric pressures due to vacuum impregnation. It is, therefore, essential to study partial discharges under these conditions. At present there is no accepted method of estimating the life of capacitor insulation under the influence of partial discharges. In the work reported here, an attempt has been made to study the partial discharge degradation of polypropylene films by conducting short-term ageing tests under sub-atmospheric pressures.

2. Experimental techniques

The following experiments were conducted:

1. Short-term ageing of polypropylene (PP) films with initial maximum discharge magnitude (Q_m) ranging from 3000 to 6000 pC. The experiments were conducted at sub-atmospheric pressures of 66·50, 33·25, 21·95, 10·00 and 4·00 kPa.
2. Measurement of electric strength over the aged area of the PP film samples.
3. Life tests where the samples were aged up to failure.

The electrodes used were Rogowski profile uniform field electrodes embedded in epoxy, except for the flat portion of the electrode surface. The sample was placed on the bottom-grounded electrode. The top electrode was separated by an airgap with the help of a suitable spacer ring, so as to produce a partial discharge inception stress of 500 kV/cm on the sample. A matching unit consisting of an RC circuit, wide-band amplifiers and a CRO were used for the detection and measurement of discharge pulses. Five decade scalers were used for pulse-height analysis. The ageing stress was 625 kV/cm which corresponded to an overvoltage of 1·25 times above the partial discharge inception voltage. The initial maximum discharge magnitude (Q_m) at the ageing voltage was controlled at a desired value by changing the impedance (non-inductive) in series with the samples without affecting the overall sensitivity of detection. The samples were microphotographed before being tested for dielectric strength. To measure the electric strength a rod-plate electrode system which was immersed in transformer oil was used. The applied voltage was increased from zero to breakdown in steps. Each sample was tested at 20 sites.

3. Main results and conclusions

(i) The ratio of the residual electric strength of the aged sample to the breakdown strength of the fresh sample is termed as RRES (relative residual electric strength). The plot of RRES of the samples aged under the same Q_m against ageing time is termed as RRES-t characteristic. An equation proposed by Simoni[2] has been fitted to the present data and lifetimes under experimental conditions are estimated (Fig. 1). These lifetimes agree reasonably well with the lifetimes obtained from lifetests, where the samples were aged till failure. Typical Weibull plots of failure times are shown in Fig. 2.

(ii) At all pressures the extrapolated lifetimes vary consistently with the initial discharge magnitude Q_m, *i.e.*, as Q_m increases lifetime decreases.

(iii) The extrapolated lifetimes for a given Q_m seem to be independent of pressure in the pressure range 66·5 to 10 kPa.

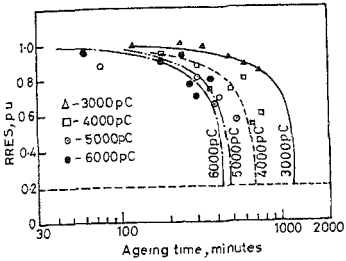

FIG. 1. RRES-t characteristic Pressure = 33·25kPa.

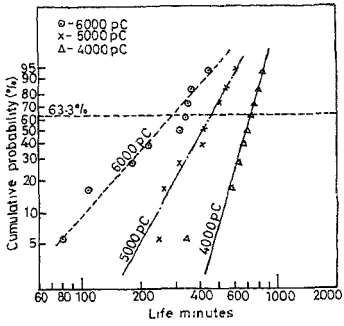

FIG 2 Weibull plots of failure times, pressure=33·25 kPa.

(iv) The voltage endurance coefficient n varies with Q_m for the same applied electrical stress. A relation has been established between n and Q_m. The value of n at 10 pC as the permissible discharge magnitude is estimated to be 11·8. This is well within the range of values of n reported in literature[3].

(v) The average value of the estimated lifetimes for each Q_m in the pressure range 66·5 to 10 kPa is calculated and an equation of the form

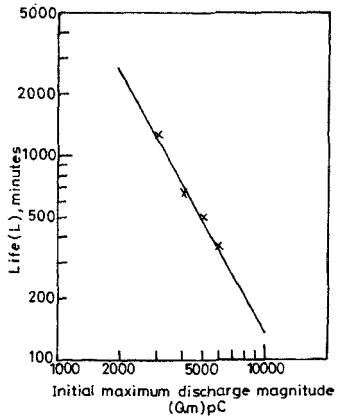

FIG. 3. L-Q_m characteristic-fitting of equation $L = AQ_m^n$.

$$L = A\ Q_m^B,$$

(where L is the average estimated lifetime, Q_m, the initial maximum discharge magnitude, A and B are the constants) has been fitted as shown in Fig 3. For a permissible discharge magnitude of 10 pC, this equation yields a life of about 57 years. This agrees reasonably well with the lifetimes of capacitors reported in the literature[4].

(vi) The total discharge magnitude/sec (Q_T) acting on the samples shows a good correlation with the extrapolated lifetimes.

(vii) The diameters of the largest pits formed due to the discharges were measured from the microphotographs. The pit diameter, in general, increases with ageing time and with increase in Q_m. The reduction in the breakdown voltage of the aged samples can be attributed to the reduction in the thickness of the films due to erosion by partial discharges.

References

1. SHAW, D. G., CICHANOWSKI, S. W., YIALIZIS, A.	A changing capacitor technology – Failure mechanisms and design innovations, *IEEE Trans.*, 1981, **EI-16**, 399–413.
2. SIMONI, L.	A new approach to the voltage endurance test on electrical insulation, *IEEE Trans.*, 1973, **EI-8**, 76–86.
3. PATTINI, G. AND SIMONI, L.	Electrical strength and voltage endurance of some insulating polymers, *Proc. IEEE Int. Symp. on Electl Insulation* (ELINSL 76) Montreal, Canada, 1976, pp 19–23
4 UMEMURA, T., ABE, K. AKIYAMA, K. AND TANAKA, Y	All-film power capacitor with folded electrode foil, *IEEE Trans.*, 1987, **PWRD-2**, 182–188

Thesis Abstract (Ph.D.)

Electron microscopy of quasicrystalline phases in aluminium-manganese and aluminium-palladium alloys by N. Thangaraj.
Research supervisors: S. Ranganathan and E. S. Rajagopal.
Department: Metallurgy.

1. Introduction

The discovery of the icosahedral phase in rapidly solidified Al-Mn alloys[1] has created a lot of interest among physicists, crystallographers and material scientists, since the icosahedral point group symmetry m $\bar{3}\bar{5}$ is incompatible with lattice translational periodicity. Because the icosahedral phase possesses 5-fold symmetry, quasiperiodicity and long-range orientational order, this phase has come to be called icosahedral 'quasicrystals'[2]. In the course of the present investigation[3] and independently[4], a new phase with two-dimensional quasiperiodicity and one-D periodicity has been found in Al-Mn alloys. Since it has 10-fold symmetry which is also incompatible with translational periodicity, it is christened decagonal quasicrystal[4]. It has been shown during the present investigation that the vacancy-ordered phases of Al-Cu-Ni and Al-Pd alloys can be considered as one-dimensional quasicrystals. The aim of the present investigation is to understand the nucleation, growth and structure of these quasicrystalline phases in Al-Mn and Al-Pd alloys.

2. Experimental procedure

Aluminium-manganese alloys with varying Mn concentrations have been chosen for the present study. Starting materials with 4N purity have been used. Al–6 at % Pd samples have been obtained in the form of melt-spun tapes from Dr H. A. Davies of Sheffield University, UK. Transmission electron microscopy (TEM) has been extensively employed to characterize the quasicrystalline phases in these alloys.

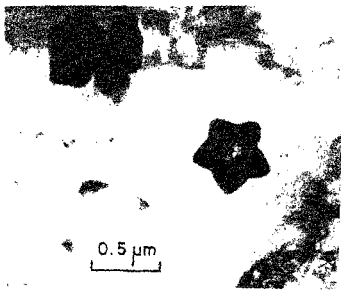

FIG. 1a The morphology of the icosahedral phase seen along the 5-fold direction – the 5-fold star in Al-5% Mn alloy

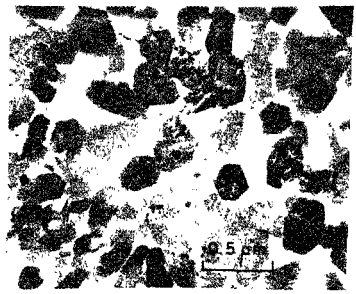

FIG. 1b The morphology of the facetted icosahedral phase in Al-14% Mn alloy viewed along the 2-fold axis

3. Icosahedral quasicrystals in Al-Mn alloys

The icosahedral phase has been found to form in Al-Mn alloys having Mn concentration as low as 5%. *The nucleation rate and the volume fraction of the icosahedral phase increases with increase in manganese* concentration. The icosahedral phase in Al-Mn alloys has been observed to display two types of morphologies, *i.e.*, non-facetted dendrites and facetted dendrites and particles. The observation of facetted quasicrystals was first reported as a result of the present study[5]. A transition from non-facetted to facetted behaviour has been observed for the icosahedral phase dendrites as the Mn concentration increases by keeping the cooling rate constant. The Mn concentration at which the transition is noticed is around 10%.

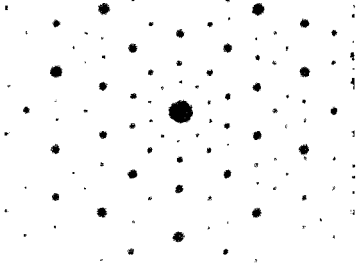

FIG. 2a. A 5-fold electron diffraction pattern obtained from Al-Mn icosahedral phase showing 3-D quasiperiodicity.

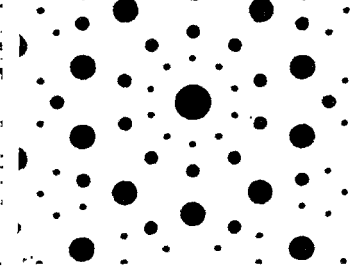

FIG. 2b The computed 5-fold diffraction pattern

Two kinds of morphologies have been observed for the icosahedral phase in Al-Mn alloys. The analysis reveals that the icosahedral phase has modified pentagonal dodecahedral growth morphology — in Al-Mn alloys with Mn concentration $\leq$ 10%. The modified shape of the pentagonal dodecahedron is essentially a twenty-pronged star-shaped solid made up of prolate rhombohedra and has icosahedral symmetry. Figure 1a shows this morphology — the 5-fold star of the icosahedral phase seen along the 5-fold axis. On the other hand, the completely facetted morphology reveals a pentagonal dodecahedral growth morphology[6] for the icosahedral phase in Al-Mn alloys with Mn concentration $\geq$ 10% Figure 1b shows the growth morphology of the facetted icosahedral particle in the Al-14% Mn alloy. In both the cases, the growth direction is found to be along the 3-fold axis.

Systematic electron diffraction experiments have been carried out to understand the structure of the icosahedral phase. Besides the electron diffraction patterns corresponding to the 5-, 3- and 2-fold symmetry zone axes reported in the original discovery, additional patterns have also been observed. The 5-fold diffraction pattern obtained from the Al-14% Mn alloy is shown in Fig. 2a. Additional important zone axes have been identified as the one corresponding to the intersection points of traces of major symmetry axes of the icosahedron, *viz.*, 5-, 3- and 2-fold. These patterns have been experimentally obtained with the exact angular relationships measured from the stereogram. The icosahedral phase diffraction patterns have also been computed by using Landau generation technique[7]. The patterns computed with the integral linear combination of vertex vectors of an icosahedron simulate the experimentally observed patterns. Figure 2b shows the computed 5-fold pattern. The subtle intensity variation observed between the experimental and computed patterns have been interpreted in terms of decoration of the underlying quasilattice by different kind of atoms or due to dynamical effects of electron diffraction patterns.

High-resolution images obtained from the icosahedral phase display quasiperiodically arranged fringe patterns[5]. The image viewed along the 5-fold symmetry axis reveals five sets of quasi-periodically spaced fringes. Their arrangement corresponds to 5-fold symmetry. Seen down the 2-fold axis the image reveals two sets of fringes each corresponding to 2- and 5-fold directions. These images rule out the possibility of multiple twinning. However, since the atomic structure of the icosahedral phase is not known, the interpretation of the high-resolution images is incomplete.

4. Decagonal quasicrystals in Al-Mn and Al-Pd alloys

The decagonal phase forms in Al-Mn alloys having Mn concentrations as low as 14% and it has been observed to coexist with the icosahedral phase. The decagonal phase nucleates epitaxially on pre-existing icosahedral phase. When the cooling rate is decreased, it is found to co-exist with crystalline Al_6Mn phase. In this case, it appears that the decagonal phase nucleates independently. The Al-Mn decagonal phase has a blocky morphology and shows characteristic striated contrast in TEM images (Fig. 3).

On the other hand, the Al-Pd decagonal phase forms as a eutectic constituent with fcc aluminium in Al-6% Pd alloy. It has been observed to co-exist with a metastable Al_2Pd phase, an orthorhombic Al_3Pd phase, and an ordered multiply twinned phase. The Al-Pd decagonal phase also shows striated contrast similar to Al-Mn decagonal phase.

Electron diffraction patterns obtained from the Al-Mn decagonal phase present a striking similarity to those of the Al-Mn icosahedral phase. The reciprocal space structure of the decagonal phase can be generated either by combination of edge vectors of an icosahedron with the introduction of mirrors or by the vertex vectors of a distorted icosahedron. Both models lead to the same reciprocal lattice for the decagonal phase. In fact, it has been theoretically proved that there is only one type of decagonal reciprocal lattice. The stereogram constructed with the edge vectors and their mirrors account for all the experimentally observed electron diffraction patterns of the decagonal phase[8]. The presence of streaks perpendicular to the 10-fold axis in the electron diffraction patterns suggests the existence of cylindrically shaped diffracting regions in real space oriented along the 10-fold axis. A typical electron diffraction pattern obtained from the decagonal phase in Al–14% Mn alloy is shown in Fig. 4.

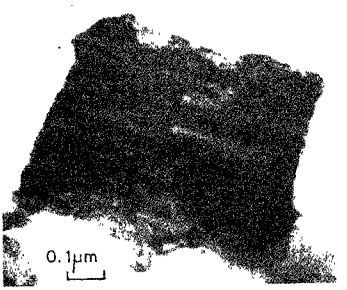

FIG. 3. The morphology of the decagonal quasicrystal in Al-14% Mn alloy showing striated contrast.

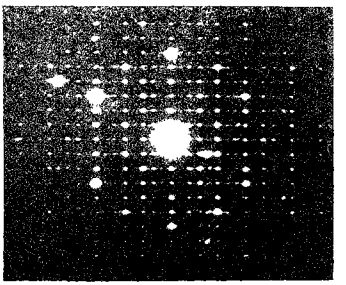

FIG. 4. A typical electron diffraction pattern obtained from the decagonal quasicrystal.

Though the Al-Pd decagonal phase gives rise to the same variety of electron diffraction patterns as that of Al-Mn decagonal phase, some subtle differences are observed. In the case of Al-Mn decagonal phase the periodicity along the decagonal axis is found to be 1·24 nm for the Al-Mn decagonal phase and 1·65 nm for the Al-Pd decagonal phase. Different levels of structural ordering has been noticed between the Al-Mn and Al-Pd decagonal phases. The arrangement of bright spots exhibited in one of the diffraction patterns follows the Fibonacci sequence (0, 1, 1, 2, 3, 5, 8....) for the Al-Mn decagonal phase and Lucas series (3, 4, 7, 11....) for the Al-Pd decagonal phase. This might be due to the compositional modulation in the decagonal lattice.

In the Al-6% Pd alloy, along with the decagonal phase, multiply twinned cubic phase and Al_3 Pd crystalline phases have been observed. Multiple twinning of such distorted cubic crystals (five of them) gives rise to a diffraction pattern with pseudo 5-fold symmetry[9]. The diffraction patterns obtained from the Al_3Pd crystalline phase bear close similarity to the one obtained from the Al-Pd decagonal phase.

5. Vacancy-ordered phases as one-dimensional quasicrystals

Vacancy-ordered τ phases observed in Al-Cu-Ni and Al-Pd alloys can be considered as one-dimensional quasicrystals[10] at the limit based on the infinite recursions of the Fibonacci sequence. A remarkable property of the vacancy-ordered τ phases is that the stacking of layers containing vacancies and transition metal atoms along the [111] directions of the rhombohedrally distorted CsCl structure follows the Fibonacci sequence. The intensity distribution of the Bragg peaks along [111] direction for a τ_{13} phase in Al-Pd alloys has been calculated by knowing the atomic positions in the layers and by the commensurate projection from two dimensions. The intensities are found to agree quite well. The intensity calculations by incommensurate projection for τ phases reveal that it is impossible to distinguish the intensity and the spacing modulation of τ phases having a repeat period of thirteen layers and above from the truly quasiperiodic τ phases. This correlation allows us to speculate that vacancy-ordering plays a role in the stabilization of quasiperiodic structures in one, two and three dimensions.

References

1 SHECHTMAN, D , BLECH, I., GRATIAS, D. AND CAHN, J W — Metallic phase with long-range orientational order and no translational symmetry, *Phys. Rev. Lett* , 1984, **53**, 1951–1953

2. LEVINE, D. AND STEINHARDT, P. J. — Quasicrystals. A new class of ordered structure, *Phys. Rev Lett.*, 1984, **53**, 2477–2480

3. CHATTOPADHYAY, K , LELE, S , RANGANATHAN, S., SUBBANNA, G N. AND THANGARAJ, N. — Electron microscopy of quasicrystals and related structures, *Curr. Sci.*, 1985, **54**, 895–903

4. BENDERSKY, L. — Quasicrystals with one-dimensional translational symmetry and tenfold rotation axis, *Phys. Rev. Lett* , 1985, **55**, 1461–1463

5. CHATTOPADHYAY, K., RANGANATHAN, S., SUBBANNA, G. N AND THANGARAJ, N. — Electron microscopy of quasicrystals in rapidly solidified Al-14% Mn alloys, *Scr Metall.*, 1985, **19**, 767–771.

6. THANGARAJ, N., CHATTOPADHYAY, K., GOPAL, E. S. R. AND RANGANATHAN, S. — On the morphology of the icosahedral quasicrystals in Al-Mn alloys, *Key Engng Mater.*, 1987, **13–15**, 245–247

7. CHATTOPADHYAY, K., LELE, S., PRASAD, R., RANGANATHAN, S , SUBBANNA, G. N. AND THANGARAJ, N. — On the variety of electron diffraction patterns from quasicrystals, *Scr. Metall.*, 1985, **19**, 1331–1334.

8 THANGARAJ, N , SUBBANNA, G. N , RANGANATHAN, S AND CHATTOPADHYAY, K — Electron microscopy and diffraction of icosahedral and decagonal quasicrystals in aluminium-manganese alloys, *J. Microscopy*, 1987, **146**, 287–302.

9. THANGARAJ, N., CHATTOPADHYAY, K , RANGANATHAN, S., SMALL, C. AND DAVIES, H.A — Quasicrystals and ordered twins in rapidly solidified Al-Pd alloys, *Proc XI Int. Conf. on Electron Microscopy*, (eds T. Imura *et al*), Vol. II, 1986, pp. 1525–1526.

10. CHATTOPADHYAY, K., LELE, S , THANGARAJ, N. AND RANGANATHAN, S — Vacancy ordered phases and one dimensional quasiperiodicity, *Acta Metall.*, 1987, **35**, 727–733.

Thesis Abstract (M.Sc. (Engng))

Finite element analysis of pyramidal and prismoidal structures by Pattabhi Sitaram.
Research supervisor: K. S. Jagadish.
Department: Civil Engineering.

1. Introduction

The behaviour of shell structures has been studied exhaustively in the literature. However, there is scanty information on the stresses in non-prismatic hipped plate structures. Pyramidal and prismoidal structures, which belong to the category of non-prismatic hipped plate structures, are examined here.

The pyramidal structure may be defined as one consisting of plane triangular plates with a common vertex at one end and a regular polygon at the other. The prismoidal structure may be considered as essentially a prismatic hipped plate with 'half pyramidal' ends at both the ends.

Some typical dimensions of pyramidal and prismoidal roof structures have been considered in this study, with a view to develop an understanding of their behaviour. Three base plans, namely, square, hexagon and octagon are considered. All the three base plans were obtained by inscribing them in a circle of radius 3·536 m. Three different rises (2·50, 3·75 and 5·0 m) are considered to study the effect of the rise/span ratio. Thus, nine different pyramids are considered for analysis. The structure is assumed to be of reinforced concrete with a thickness of 5 cm. Only symmetrical dead and live loads are considered.

Two typical prismoidal roofs are considered to cover a rectangular plan dimension of 6·0 × 3·5 m. The first one is a hipped and gabled type of prismoid with a rise of 1·5 m. The second one has a flattened top with a rise of 1·07 m.

2. Analysis

The present analysis is limited to symmetrical loadings. Accordingly, the symmetry of the problem has been exploited to reduce the size of the problem. In the case of the pyramid, this could be achieved by considering one half of the triangular faces. In the first prismoidal structure, halves of two dissimilar adjacent faces, among the four faces, can be considered. In the second prismoid, halves of three dissimilar adjacent faces can be considered.

The problem, reduced in this fashion, is now taken up for a finite-element analysis. Two-dimensional, parabolic isoparametric elements are considered. It represents a flatshell kind of element considering in-plane deformation and plate bending. To facilitate the assembly of neighbouring elements which are not co-planar, a fictitious twisting rotation is also defined.

The equations of equilibrium of the problem are now solved through the frontal technique, wherein the formation of the equations and the elimination of the variables proceed simultaneously. The resulting displacements are then used to obtain the stresses and the stress resultants in each element. Two approximate analyses are also considered to facilitate the understanding of the physical behaviour of the structures. In the first approach, the pyramid is considered as an assembly of plates with the ridges supported and fixed against rotation. This would mean that the deflections at the ridges are ignored and purely a plate bending behaviour is considered. In the second, a membrane analysis is considered, mainly using the in-plane stress σ_y which is in equilibrium with the dead and live loads above a particular section.

3. Results

In all the pyramidal structures, the vertical deflection w is negligible at the apex and at the ridges. The deflection values increase as one moves away from the ridges. The maximum deflection occurs on the line $x = 0$, at some point at a height in the range 0·25 to 0·375 H. The in-plane stresses σ_x and σ_y are generally compressive except in the square pyramid with the lowest rise. The stress σ_y is closely approximated by the simpler membrane stress for all the pyramids considered. (The x-axis coincides with the base of the triangle while the y-axis is along the perpendicular from the vertex on the base.) σ_y is generally larger than σ_x and its value reaches a maximum at the base.

The bending moment M_x is generally positive in the interior of each face of the pyramid. It, however, attains a negative value near the ridge. The variation of the bending moment closely follows that in a triangular plate. The maximum value of the moment M_y is generally smaller than the maximum value of M_x and the variation is similar to that in a triangular plate. It is interesting to observe that M_y decays roughly exponentially in the y direction, analogous to the behaviour in conical shells.

The results for the prismoidal roofs show that the in-plane (membrane) stresses are generally small when compared with the flexural stresses. The lateral deflection and bending moments decrease considerably as the number of plates is increased from 2 to 3.

References

1. CHANDRASHEKARA, K. AND MADHAVA RAO, M. S. — Stress analysis of pyramidal hipped plate structure, *Bldg Sci.*, 1970, **5**, 153–159.
2. TERRINGTON, J. S. — *Design of pyramid roofs*, 1957, Concrete Publications, London.
3. BORN, J. — *Hipped plate structures*, 1962, Crosby Lockward, London.
4. IRONS, B.M. — A frontal solution program, *Int. J. Num. Meth. Engng*, 1970, **2**, 115–132.
5. HINTON, E. AND OWEN, D. R. J. — *Finite element programming*, 1977, Academic Press.

Thesis Abstract (M.Sc. (Engng))

Some studies on automatic-repeat-request error-control schemes by D. S. Babu.
Research supervisor: T. S. Vedavathy.
Department: Electrical Communication Engineering.

1. Introduction

In high-speed data communication, error-detecting and error-correcting codes become an integral part of the design since it is important to deliver an error-free information to the destination. ARQ Scheme is one of the basic categories of error-control schemes for data communication. This scheme basically aims at minimising the block error probability for an optimum throughput efficiency. There are different types of ARQ schemes[1] which aim at better throughput performance. In this work, a detailed study of these schemes has been reported. A new type of modified and generalized stop-and-wait ARQ schemes is worked out. It is proved that this scheme yields better throughput performance than the one which was recently proposed by Moeneclaey *et al*[2].

2. Improved optimum generalized stop-and-wait scheme

In the optimum generalized stop-and-wait ARQ scheme the transmitter sends an optimum number of identical copies of a data block rather than a single copy and waits for the positive acknowledgement from all the copies sent. In the scheme proposed, the transmitter does not wait for the acknowledgements, but starts sending an optimum number of copies of the next block. This is shown to improve the throughput efficiency. The operation of the proposed scheme is illustrated in Fig. 1. Whenever a block of data is to be sent, an optimum number m copies of the block is transmitted. If the first received copy of the block is error-free, ACK is sent and the succeeding m-1 copies are rejected. If not, NAK is received and the receiver checks the second copy. This process continues till at least one ACK is received, soon after which the transmitter sends the next data block.

It is assumed that block errors occur independently with a probability p and the number of copies of the data block to be sent for maximum throughput is optimized. This optimum number is shown to be a function of p for a given round-trip-delay s.

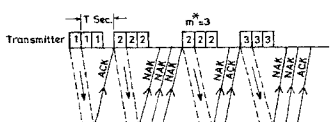

FIG. 1. Modified optimum generalized stop-and-wait ARQ scheme (Asterisk denotes that the receiver discards these copies).

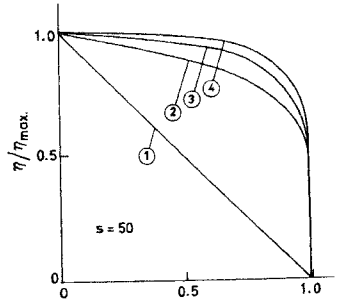

FIG. 2. Throughput comparison (s = 50). 1. Conventional; 2. Opt. generalized; 3. Modified opt. generalized (case 1, $m^*_{MO} = m_O$); 4. Modified opt. generalized (case 2, $m^*_{MO} = m_O$)

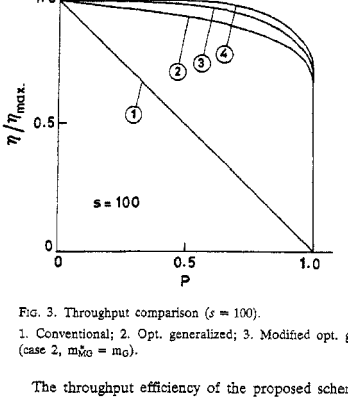

FIG. 3. Throughput comparison ($s = 100$).

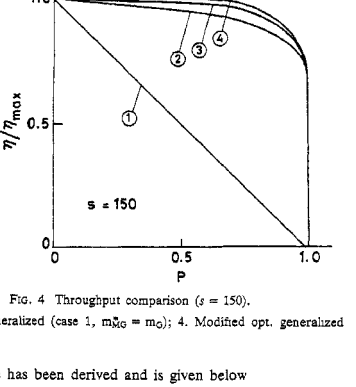

FIG. 4 Throughput comparison ($s = 150$).

1. Conventional; 2. Opt. generalized; 3. Modified opt. generalized (case 1, $m_{MG}^{*} = m_O$); 4. Modified opt. generalized (case 2, $m_{MG}^{*} = m_O$).

The throughput efficiency of the proposed scheme has been derived and is given below

$$\eta_{MG} = \frac{\eta_{max}\,(1+S)\,(1-P)\,(1-P^m)}{(1-P^m) + S(1-P)}$$

where η_{max} is the theoretical upper bound given by

$$\eta_{max} = \frac{k}{(n + RT)}$$

where k is the number of information bits per block, R the transmission rate in bits per second and T the round-trip delay in seconds which is the time elapsed between the transmission of a data block and the reception of the ACK. n is the total number of bits per block and $S = RT/n$.

Figures 2–4 show the comparison of throughput efficiency of the proposed scheme with that of the other existing ARQ schemes for different values of s.

3. Conclusion

It is observed that the throughput efficiency of the proposed scheme is higher than that of the other schemes. Also, the receiver, after accepting a copy of the data block as error-free, discards the succeeding copies of the data block. It is also observed that the throughput is almost constant over the entire region of the block error probability and is almost insensitive to it. These results show the effectiveness of the proposed scheme. This scheme can be practically simulated.

References

1. BABU, D. S. AND VEDAVATHY, T. S. — Improving the optimum generalized stop-and-wait ARQ scheme, *Electronics Lett.*, 1986, **22**, 649–650.

2. MOENECLAEY, M., BRUNEEL, H., BRUYLAND, I. AND CHUNG, D.Y. — Throughput optimization for a generalized stop-and-wait ARQ scheme, *IEEE Trans.*, 1986, **COM-34**, 205–207.

Thesis Abstract (M.Sc. (Engng))

Random jumps of a Duffing oscillator under narrow-band random excitation by N. G. Vijaya Vittala.
Research supervisor: G. V. Anand.
Department: Electrical Communication Engineering.

1. Introduction

The Duffing oscillator serves as a good model for a class of nonlinear vibrating systems with nonlinear stiffness and linear damping characteristics. It is well known that the harmonic response of a Duffing oscillator to sinusoidal excitation exhibits the phenomenon of multivalued response and jumps. Studies of the response of a Duffing oscillator to stationary Gaussian random excitation have shown that the mean-square response becomes multivalued and exhibits random jumps from one state to another if the excitation bandwidth is sufficiently small[1,2]. But no investigation regarding the statistics of the jumps, such as the *average time interval between jumps, the average fractional occupation time of the different states, etc.*, is available in literature. Information about the statistics of the jump phenomenon is necessary for a complete understanding of the nature of the response and is particularly important for obtaining an estimate of the fatigue damage accumulated by the system. The work presented here seeks to fill this gap.

2. Excitation plane analysis

Before proceeding to analyse the statistical characteristics of these random jumps it is instructive to take a close look at the jump phenomenon under sinusoidal excitation with reference to Fig. 1. In this figure the response amplitude A is plotted as a function of the excitation amplitude f for different values of excitation angular frequency ω. If ω is less than a certain critical value ω_{min}, the response amplitude A is a single-valued function of f for all f. On the other hand, A is a triple-valued function over a certain range of values of f when $\omega > \omega_{min}$. In this case, the upper and lower branches of the response curve represent stable states and the middle branch represents an unstable state. For a given $\omega > \omega_{min}$ the response is multivalued if f satisfies the condition $f_1(\omega) < f < f_2(\omega)$. The response exhibits a jump whenever the amplitude f or frequency ω of the excitation crosses a critical value, the critical value for the downward jump being different from that for the upward jump. We define the ω–f plane as the excitation plane, and designate a point (ω,f) in this plane as the excitation point. The loci of points in the excitation plane at which the up/downward jump occurs divide the excitation plane into four regions, designated as D_s, D_m, D_u and D_l. This partitioning with the inequalities defining the respective regions is shown in Fig. 2. If the excitation point lies in the region D_u, the response amplitude A lies on the

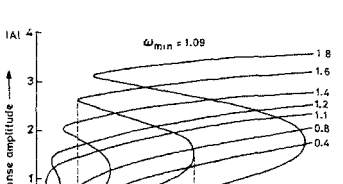

FIG 1. Family of response curves for a Duffing oscillator as a function of excitation amplitude for different values of excitation frequency.

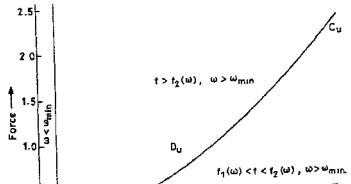

FIG. 2. Demarcation of regions D_s, D_m, D_l, and D_u in the excitation plane

upper branch of the response curve, *i.e.*, in the higher state. If the excitation point lies in the region D_l the response amplitude A lies on the lower branch of the response curve, *i.e.*, in the lower state. If the excitation point is in the region D_m, the response may be either in the higher or the lower state. This region with an upper boundary C_u and a lower boundary C_d is the region of multivalued response. A transition of the response from the higher to the lower state, accompanied by a downward jump of the response amplitude, occurs when the excitation point (f,ω) leaves the region D_m by crossing the lower boundary C_d. A transition from the lower to the higher state, accompanied by an upward jump of the response amplitude, occurs when the excitation point (f,ω) leaves the region D_m by crossing boundary C_u. Finally, the region D_s defined by $\omega < \omega_{min}$ is a region of single-state response for all values of f.

3. Narrow-band excitation

A narrow-band excitation can be represented as a quasisinusoidal excitation whose amplitude $f(t)$ and frequency $\omega(t)$ are slowly varying random functions of time. Hence, the excitation point traces a random trajectory in the excitation plane, and random jumps occur whenever the trajectory crosses from D_l to D_u *via* D_m or from D_u to D_l *via* D_m. If the excitation is a sample function of a narrow-band Gaussian random process, the functions $f(t)$ and $\omega(t)$ are sample functions of the jointly stationary random processes $F(t)$ and $\Omega(t)$ whose joint probability density function is given[3] by eqn 1.

$$P_{F,\Omega}(f,\omega) = (f^2/\sigma^3 B\sqrt{2\pi}) \quad \exp\{-[(\omega-\omega_c)^2 + B^2]f^2 / 2\sigma^2 B^2\},\ f \geq 0 \tag{1}$$

where ω_c is the centre frequency, σ^2 the intensity and B the bandwidth of the excitation. Integrating the joint probability density function over the appropriate regions of the excitation plane, the probabilities of the regions D_s, D_l, D_m and D_u are determined as

$$P_i = P(D_i) = \int_{D_i}\int P_{F,\Omega}(f,\omega)\, df\, d\omega \tag{2}$$

where $i = s,m,l,u$.

These probabilities have been determined for three different spectra of the excitation process, *viz.*, (1) a Gaussian spectrum, (2) a resonant filter spectrum, and (3) a flat top (ideal filter) spectrum. The probability is computed and plotted as a function of the centre frequency of excitation for different values of the excitation mean-square amplitude and bandwidth, and also for the different values of the system parameters. These results give us a valuable insight into the behaviour of the excitation trajectory.

3. Fractional occupation times and mean excursion durations

Transitions of response from one state to another can also occur without jump if the excitation trajectory goes from D_l to D_u or from D_u to D_l *via* the region D_s. But the probability of such an occurrence is very small if $|\omega-\omega_{min}| > B$, where B is the bandwidth of the narrow-band process. Hence, unless ω_c lies in the very small interval $(\omega_{min} - B,\ \omega_{min} + B)$, the possibility of a transition without jump can be ignored. Referring to individual sample functions of the response, the fractional occupation times of the higher and lower states are denoted by P_{HS} and P_{LS}, respectively, while the lower state are represented as $E[T_h]$ and $E[T_l]$. Expressions for these averages have been derived by initially ignoring the fluctuations of the instantaneous frequency and treating the problem as a level-crossing problem of the envelope of the excitation process[4]. To take the variations of instantaneous frequency into account, the results thus obtained are averaged over frequency. The average fractional occupation time and the average occupation time per excursion for the two states have been plotted as a function of the centre frequency for the three types of excitation spectra mentioned in the last paragraph and for several values of the mean-square excitation amplitude σ^2, fractional bandwidth B_f, nonlinearity parameter h, and damping factor k (Figs 3 and 4). Knowledge of P_{HS}, P_{LS}, $E[T_h]$ and $E[T_l]$ would be particularly useful in the statistical analysis of cumulative fatigue damage of structures subjected to narrow-band random excitation.

4. Random jumps of nonlinear strings

The analysis has been further extended to single-mode nonlinear vibrations of a string represented by a pair of nonlinearly coupled Duffing equations. The boundary of the multivalued response region D_m in

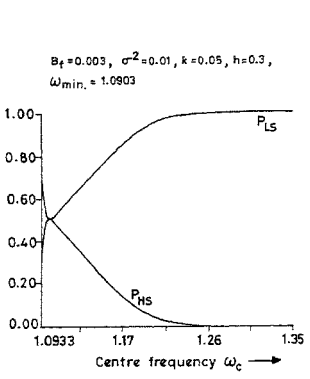

3. Probability of finding the response in different states.

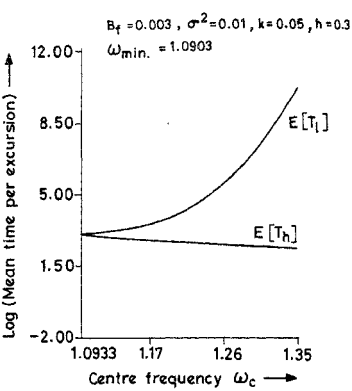

FIG. 4. Mean time per excursion for different states.

excitation plane has been determined taking into account modifications due to the nonplanar response he string. Experimental results have also been obtained by subjecting a string fixed at the ends to a row-band Gaussian excitation. The experimental set-up consists of a stretched brass string connected a narrow-band current source and subjected to a constant high magnetic field at the centre. The tation current is obtained by passing a wideband Gaussian signal through a narrow-band filter with a tly flat top and a very rapid roll off outside the pass band. The centre frequency and the bandwidth he filter are adjustable. The string vibrations are picked up using a capacitance pick up and recorded a level recorder. The output of the level recorder, presented for different values of the centre fre- ıcy and the bandwidth, clearly indicates the occurrence of the random jumps. The measured values ıe mean fractional occupation time and the mean occupuation time per excursion for the two response s agree fairly well with the theoretical predictions.

rences

ICHARD, K AND ANAND, G. V.	Non-linear resonance in strings under narrow band random excitation, *J. Sound Vibr.*, 1983, **86**, 85–98.
AVIES, H. G. AND NANDLAL, D.	Phase plane for narrow band random excitation of a Duffing oscillator, *J. Sound Vibr.*, 1986, **104**, 277–283.
AVENPORT, W. B. AND OOT, W. L.	*An introduction to the theory of random signals and noise*, Ch. 8, 1958, McGraw-Hill.
IGAM, N. C.	*Introduction to random vibrations*, Ch. 6, 1983, MIT Press.

is Abstract (M.Sc. (Engng))

ies on metal-oxide-semiconductor structures on polycrystalline silicon by M. V. akshmi.
arch supervisor: K. R. Ramkumar.
artment: Electrical Communication Engineering.

roduction

ystalline silicon (polysilicon) is extensively employed in integrated circuit technology. Layers of

polysilicon have been found to be economically attractive in the fabrication of high-value resistors (in static memory devices) and as gate electrodes in metal-oxide-semiconductor (MOS) structures[1].

Considerable amount of work has been reported on the microstructure of grain boundaries and carrier transport in polycrystalline semiconductors. However, investigations on polysilicon devices are generally limited to solar cells. Polycrystalline silicon is a low-cost material which can be explored for device applications. The present investigation has been undertaken to study the MOS structure on polysilicon. The main objective is to understand the characteristics of the polysilicon-polyoxide interface for possible device applications.

2. Fabrication and characterisation

The capacitance-voltage (C-V) measurements on these MOS structures revealed that the oxide on polysilicon is highly conductive. Therefore, an attempt has been made to study in detail the current-voltage (I-V) characteristics of the MOS device. MOS test structures have been fabricated using polysilicon wafers. The average thickness of the oxide layer (grown by thermal oxidation) ranges from 1000 to 2000Å.

The I-V characteristics of the MOS devices are measured for both polarities of the applied voltage. The measurements are repeated at different temperatures. The I-V characteristics indicate that the MOS devices which are located well within a grain show negligible conduction throughout the voltage and temperature ranges considered. However, devices which contain grain boundaries show significant conduction and nonlinear I-V characteristics. Further, these characteristics are sensitive to the polarity of applied voltage and ambient temperature (Figs 1 and 2).

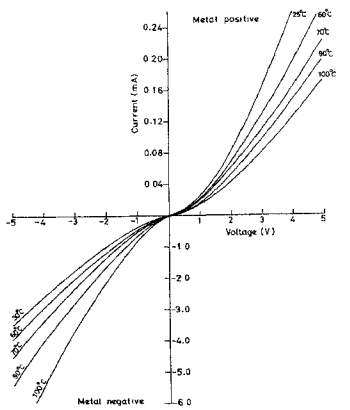

FIG. 1. Measured I–V characteristics with temperature.

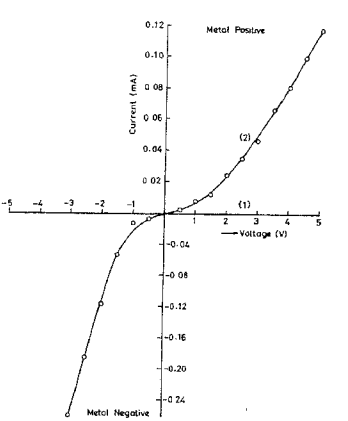

FIG. 2. Experimentally obtained I–V characteristics. Device (1) inside a grain and (2) on the grain boundary.

3. Analysis

Several theoretical models have been reported in literature to explain the conduction through oxides grown on polycrystalline silicon (polyoxides). These are generally based on the local enhancement of the electric field in the oxide due to rough texture at the interface and the resultant Fowler-Nordheim (F-N) tunneling at localised regions. It appears that the conduction behaviour observed is difficult to explain by F-N tunneling because the oxide thickness is very large (> 1500 Å) and the applied voltages are small compared to those reported. Also the above models cannot explain the I–V characteristics at different temperatures.

It is felt that the grain boundary traps in the polyoxide might be playing a vital role in deciding the carrier transportation through the oxide. The measurements show that the current flow in the device is restricted to the oxide in and around the grain boundaries. It is proposed that the carriers from the metal (or the semiconductor) tunnel through the oxide to the trap levels in the grain boundaries. The trapped carriers move by impurity band conduction (hopping mechanism)[2] and reach the other side of the oxide (semiconductor or metal). Thus electrons get transported across the oxide and contribute to current flow. As the bias voltage is increased the number of electrons which get into the oxide traps by tunneling also increases. This gives rise to the observed nonlinear I–V characteristics. With change in polarity of the applied voltage, the source of injection of electrons into the oxide traps changes; hence, the magnitude of the current flow varies. Further, with increase in temperature, the carrier concentration increases in the semiconductor and the Fermi level gets shifted. Therefore, the I–V characteristics get affected.

Based on the above model, current values have been computed for various voltages considering the tunneling probability and carrier trapping. The computed I–V characteristics agree satisfactorily with the observed characteristics indicating the validity of the model proposed above.

. Impedance *vs* frequency characteristics[3]

We felt that the grain boundary resistance in conjunction with the MOS capacitance (inside a grain) may lead to interesting variation in the impedance of the structure with frequency (Z *vs* f). Systematic Z *vs* measurements have been carried out for different values of dc bias and both polarities of the applied voltage. The measurements indicate that the impedance remains fairly constant at low frequencies but decreases beyond a certain frequency. As the dc bias is increased the impedance value comes down but the frequency at which the impedance starts decreasing, increases (Fig. 3).

With a view to understand the impedance frequency characteristics, the knowledge of dc V–I characteristics of the sample have been used. The MOS structure has been represented as a distributed RC network consisting of resistance and capacitance offered by the space charge region in the semiconductor,

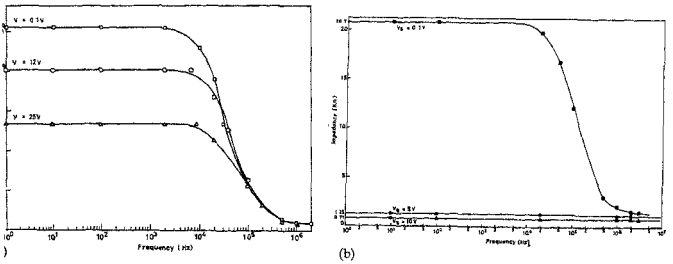

g 3. Variation of impedance with frequency for different dc bias voltages for (a) metal positive, and (b) metal negative aracteristics when metal is positive.

the oxide and the bulk. The variation of impedance with frequency of several samples has been computed based on the equivalent circuit and these variations are found to be in good agreement with the experimental values.

The impedance variations discussed above indicate that the MOS structure on polysilicon exhibits impedance-frequency characteristics similar to that of a low-pass filter.

5. Conclusions

These investigations indicate that the abnormally large conduction exhibited by the MOS structure on polysilicon can be exploited to conceive variable resistors, voltage/current low-pass filters, etc.

References

1. SZE, S. M. — *VLSI Technology*, 1983, McGraw-Hill.
2. TANIGUCHI, M., HIROSE, M., OSAKA, Y., HASEGAWA, S. AND SHIMIZU, T. — Current transport in doped polycrystalline silicon, *Jap. J. Appl. Phys.*, 1980, **19**, 665–673.
3. LAKSHMI, M. V. S. AND RAMKUMAR, K. — Impedance-frequency characteristics of metal-oxide-semiconductor structures on polycrystalline silicon, *J. Appl. Phys.*, 1988, **63**, 934–937.

Thesis Abstract (M.Sc. (Engng))

Electrochemical aspects of grinding media wear with respect to base metal sulphides

by Vathsala.
Research supervisor: K. A. Natarajan.
Department: Metallurgy.

1. Introduction

Flotation is a well-known beneficiation process especially for sulphide minerals. Grinding in steel rod and ball mills is an essential and unavoidable procedure preceding such a concentration process. An estimated over 50,000 tonnes of steel is consumed each year around the world as grinding media in the wet grinding of minerals[1]. Grinding media wear is believed to result from poorly understood complex interactions among corrosion, abrasion and impact. The corrosion component of the media wear was found to be a function of the mineral in the slurry[2-4]. It has also been observed that grinding media wear is about 5–10 times greater in wet grinding than in dry grinding[5]. No systematic study on grinding media wear has so far been reported in India. However, it has been known that wear of grinding balls is an enormous problem facing the Indian mineral processing industries. It could be estimated that even if the ball wear is reduced by a small percentage, considerable saving in grinding could be achieved.

Grinding media-mineral interactions inside the ball mill besides contributing to the ball wear could also affect the surface properties of the ground minerals, thereby influencing their flotability. It has been reported that the flotability of sulphide minerals is signficantly affected by the nature of the grinding media and by the type of conditions used[6-8].

The main objectives of this work are:

i) Establishment of the electrochemical and corrosion characteristics of different ball materials under different conditions.

ii) Investigation of the grinding media-mineral galvanic interaction with respect to the flotation of sphalerite.

2. Experimental programme

The individual electrode potentials as a function of pH and aeration, combination potentials and galvanic currents for the different possible combinations of a hypersteel grinding medium and sulphide minerals were measured to understand the electrochemical behaviour of the various ball materials (both cast and forged hypersteel) and of the sulphide minerals (pyrite, chalcopyrite, galena and sphalerite) under open circuit conditions. Steady-state polarization studies were carried out to understand the electrochemical behaviour for all the ball material and sulphide mineral electrodes under applied potential conditions. Corrosion rates of different ball materials in the presence and absence of a mineral slurry were estimated and the various materials classified accordingly. Corroded ball material surfaces after anodic polarization in the presence of both pyrite and galena slurries under oxygenated conditions have been examined through scanning electron microscopy (SEM).

The galvanic interaction between a hypersteel grinding medium and sphalerite, and its effect on flotation has been brought out. Flotation of sphalerite was carried out in the presence and absence of a collector and/or an activator while contact under oxygenated and deoxygenated conditions; and the recovery has been calculated and compared.

3. Main results and conclusions

The measured rest potentials for the various sulphide minerals and ball materials are dependent on the oxygen levels in solution. An arrangement of the various sulphide minerals and the ball materials in their increasing order of activity under all aeration conditions, irrespective of the type of electrolytes used, gives the following series:

Pyrite	
Chalcopyrite	
Galena	
Sphalerite	
Kudremukh megattaux	Increasing activity
High chrome cast iron	
EN31	
EN44	
Darbia material	
Hypersteel	

A combination (mixed) potential was found to be established whenever two dissimilar (sulphide mineral and Dariba ball material) electrodes came into contact. Under such combinations, the dissolution of the ball material was found to be increased. In general, relatively high galvanic currents were observed in couples containing two dissimilar electrodes which are placed farther apart in the galvanic series.

Various ball materials and sulphide minerals exhibited passive and transpassive regions during anodic polarization in 0·5 M H_2SO_4 (pH 0·2–0·25).

The corrosion rates for the ball materials were found to be relatively higher in the presence of galena and pyrite slurries especially with added availability of oxygen. The ball materials exhibited deeper pitting on their surfaces after anodic polarization in the presence of pyrite and galena slurries.

SEM examinations of the corroded ball surfaces after anodic polarization in the presence of galena and pyrite slurries under oxygenated conditions revealed surfaces with exfoliations, fissures and cracks, numerous pits and corrosion products. Figure 1 depicts a scanning electron micrograph of the corroded Dariba ball material in the presence of a pyrite slurry.

Prior galvanic contact between the sphalerite mineral and a Dariba (hypersteel) grinding medium deleteriously affects the flotation response of the sphalerite; the presence of oxygen during such galvanic

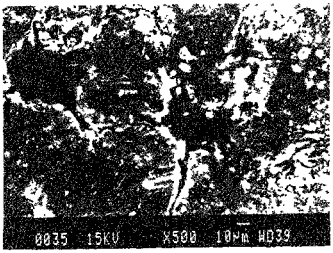

FIG. 1 Scanning electron micrograph of the Dariba ball material after anodic polarization in the presence of a pyrite slurry.

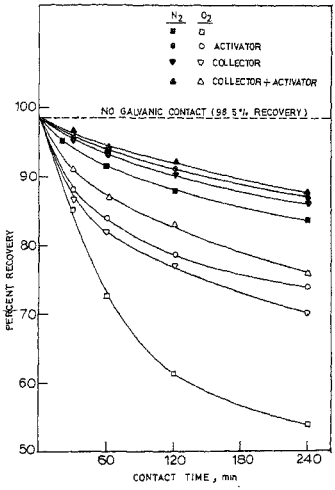

FIG. 2 Flotation recovery of sphalerite after galvanic contact with hypersteel ball in the presence and absence of collector and/or activator

contact further decreasing the recovery. The presence of collector and activator while in galvanic contact appears to minimise such a deleterious effect. Typical results of the flotation tests are depicted in Fig. 2.

References

1. REMARK, J F AND WICK, O. J — Corrosion control in ball and rod mills, Paper 121, *Corrosion 76*, NACE, Houston, Texas, 1976.
2. LUI, A W. AND HOEY, G R — Corrosive and erosive wear of metals in mineral slurries, *Can Metall.*, 1973, **12**, 185–190
3. LUI, A W. AND HOEY, G R — Corrosion inhibitors for the reduction of wear in iron ore grinding, *Mater Performance*, 1976, **15**(9), 13–16.
4. LUI, A W AND HOEY, G R — Use of alkaline additives to reduce wear on steel balls in grinding low grade copper ore, *Br Corros. J*, 1977, **12**(1), 51–53
5. BOND, F. C. — Wet *versus* dry grinding, *Min. Cong. J*, 1957, **43**(1), 38–41.
6. REY, M AND FORMANEK, V. — Some factors affecting the selectivity in the differential flotation of lead-zinc ores in the presence of oxidized minerals, *Proc. 5th Int. Miner. Process Congr*, Inst Min. Metall., London, 1960, p 343.
7. THORNTON, E — The effect of grinding media on flotation selectivity, *Proc. 5th A. Meet Can. Miner Process*, Ottawa, Ont, 1979, p. 224
8. IWASAKI, I., REID, K. J., LEX, H. A AND SMITH, K. A. — Effect of autogenous and ball mill grinding on sulphide flotation, *Min. Engng.* 1983, **35**, 1184–1190.